Check for updates

International Journal for Numerical Methods in Engineering

WILEY

RESEARCH ARTICLE OPEN ACCESS

Numerical Stability of Soil-Water Coupled Analysis With Implicit Time Integration Using Spectral Radius of Recursive Equation Comprising Discretized Governing Equation of *u-p* Formulation

Tomohiro Toyoda | Toshihiro Noda

Nagoya University, Nagoya, Japan

Correspondence: Tomohiro Toyoda (toyoda@civil.nagoya-u.ac.jp)

Received: 21 August 2025 | **Revised:** 30 September 2025 | **Accepted:** 9 October 2025

Funding: This work was supported by JSPS KAKENHI (Grant Number 22K14324).

Keywords: high permeability | numerical instability | soil-water coupling | spectral radius | ***u-p*** formulation

ABSTRACT

The numerical stability of the ***u-p*** formulation-based dynamic soil-water coupled analysis was evaluated using the spectral radius of a simultaneous recursive equation derived from the spatiotemporally discretized governing equations and time-integration formulas. The findings reveal that the unstable range of the ***u-p*** formulation forms a band-shaped region in the permeability coefficient k-time increment Δt space. This band bends at the point where the theoretical solution of the ***u-p*** formulation transitions. By analyzing the transience of the eigenvector along the band, we identified significant eigenvector rotation around the bend, suggesting that the differing appearances of unstable regions between low- and high-permeability ranges are caused by variations in the divergence of eigenmodes. Moreover, the criterion proposed by Noda et al. (2008) for evaluating the feasibility of ***u-p*** formulation-based analysis, which relies on the ratio $k/\Delta t$, is generally valid for low-permeability ranges. However, this criterion proves inconsistent for high-permeability ranges, where feasibility depends solely on Δt.

1 | Introduction

Soil-water coupled analyses of saturated soil as a two-phase mixture [1–3] have traditionally been conducted using the ***u-p*** formulation (hereafter abbreviated as "***u-p***"), which assumes static seepage of pore water, as formulated by Zienkiewicz et al. [4]. This assumption effectively reduces the number of unknown variables but causes numerical divergence in highly permeable soils that allow dynamic seepage [5], despite the theoretical solution of the ***u-p*** formulation exhibiting unconditional convergence [6]. This numerical instability can be addressed by employing the Full formulation (hereafter abbreviated as "*Full*"), such as the ***u-U-p*** formulation or the ***u-U-p***/***u-w-p*** formulation [7–11], which accounts for dynamic pore water flow, or the ***u-U***/***u-w*** formulation [11–13], which further incorporates pore water compressibility.

This is an open access article under the terms of the Creative Commons Attribution-NonCommercial License, which permits use, distribution and reproduction in any medium, provided the original work is properly cited and is not used for commercial purposes.

© 2025 The Author(s). *International Journal for Numerical Methods in Engineering* published by John Wiley & Sons Ltd.

The numerical instability of the $\boldsymbol{u}$-p formulation has been widely discussed in previous studies. Zienkiewicz et al. [4] were the first to compare solutions derived from Biot's theory (*Full*), the $\boldsymbol{u}$-p formulation, and the static consolidation theory for a one-dimensional saturated elastic soil column under periodic surface loads. They identified deviations of the $\boldsymbol{u}$-p formulation from *Full*, particularly in highly permeable ranges (with greater π_1 values) and high-frequency ranges (with greater π_2 values), due to the limitations of the $\boldsymbol{u}$-p approximation. However, their work did not address the numerical instability arising in the temporally discretized system, that is, instability dependent on the time increment Δt. Noda et al. [5] proposed a simple criterion to evaluate the feasibility of $\boldsymbol{u}$-p calculations based on the spatiotemporally discretized soil-water coupling equation (SWCE). They suggested that $\boldsymbol{u}$-p-based numerical simulations fail due to the sign inversion of the discretized SWCE when the coefficient $\gamma_{\theta 1}$ becomes negative. This occurs in cases of highly permeable soils (large permeability coefficient k) or for rapid phenomena requiring sufficiently small Δt, such as failure problems or high-frequency soil seismic responses. The stability criterion they proposed is expressed as:

$$\gamma_{\theta 1} = \frac{1}{6} - \frac{1}{2\theta \Delta t} \frac{\rho^f k}{\gamma_w} > 0, \quad \frac{k}{\Delta t} < \frac{\theta \gamma_w}{3\rho^f} \ldots \text{Stable} \tag{1}$$

where θ is the parameter introduced in Wilson's θ method (hereafter abbreviated as "*Wilson-θ*") proposed by Wilson et al. [14]. ρ^f and γ_w are the pore water density and the pore water unit weight, respectively, indicating that $\boldsymbol{u}$-p-based calculations fail when $k/\Delta t$ exceeds a critical threshold. However, this study did not evaluate the stability of the entire discretized system, including the equation of motion (EOM). Kato [15] derived a stability criterion using Routh's [16] and Hurwitz's [17] stability criteria in conjunction with Newmark's β method [18] as:

$$\epsilon > \frac{k}{g \Delta t} \ldots \text{Stable} \tag{2}$$

where g represents gravitational acceleration, ϵ is a parameter satisfying $1/2 > \epsilon > 0$. However, this study only considered a single mass point in a one-dimensional domain, neglecting spatial discretization effects.

Other studies have explored the stability of direct time integration methods. Newmark [18] demonstrated that appropriate parameter settings (e.g., the average constant acceleration method) ensure unconditional convergence. Bathe and Wilson [14] analyzed the numerical stability of the *Wilson-θ* and Newmark's β methods (hereafter abbreviated as "*Newmark-β*") using the spectral radius of the temporally discretized governing equation. They concluded that *Wilson-θ* achieves unconditional convergence when $\theta > 1.37$. However, these studies focused solely on linear second-order equations of motion for single or multiple mass points. They did not address boundary value problems or the effects of soil-water coupling on system stability.

In this study, the stability of dynamic $\boldsymbol{u}$-p-based soil-water coupled analyses was evaluated using the spectral radius of a simultaneous recursive equation derived from the spatiotemporally discretized $\boldsymbol{u}$-p governing equations and time integration formulas (primarily *Wilson-θ*, supplemented with *Newmark-β*). The analysis identified the stable range of the $\boldsymbol{u}$-p formulation based on k and Δt, revealing that instability induced by the $\boldsymbol{u}$-p approximation can occur even with parameters deemed unconditionally stable under *Wilson-θ*. Furthermore, we confirmed that the $\gamma_{\theta 1}$ criterion proposed by Noda et al. [5], which depends on $k/\Delta t$, is valid only for low-permeability cases and is inconsistent for highly permeable cases. Finally, we demonstrated that the differing appearances of the stable ranges between low- and high-permeability cases result from significant changes in the divergence of eigenmodes near the transience of the theoretical solution of the $\boldsymbol{u}$-p formulation.

The governing equations and the stability evaluation scheme are summarized in Section 2. The investigation of the stable range of $\boldsymbol{u}$-p is presented in Section 3, followed by supplementary discussions in Section 4. Conclusions are presented in Section 5.

2 | Governing Equations and Scheme for Evaluating Numerical Stability

In this section, the governing equations of the $\boldsymbol{u}$-p formulation are presented along with their discretized form, and the scheme for evaluating numerical stability using the spectral radius is introduced. The derivation of the governing equations and their theoretical solutions follows the methodology outlined by Toyoda and Noda [6].

10970207, 2025, 21, Downloaded from https://onlinelibrary.wiley.com/doi/10.1002/nme.70164 by Nagoya University, Wiley Online Library on [07/10/2026]. See the Terms and Conditions (https://onlinelibrary.wiley.com/terms-and-conditions) on Wiley Online Library for rules of use; OA articles are governed by the applicable Creative Commons License

2.1 | *u-p* Governing Equation

2.1.1 | Original Governing Equation

According to Noda and Toyoda [7], the *full-based* governing equations, including the "rate-type" EOM for considering geometrical/convective nonlinearity, were indicated as follows [11, 19]:

EOM of mixture (rate-type [7]):

$$\rho_s \mathrm{D}_s^2 \boldsymbol{v}_s + \rho_f \mathrm{D}_s \mathrm{D}_f \boldsymbol{v}_f + \rho^f \left(\operatorname{div} \boldsymbol{v}_s\right)\left(\mathrm{D}_s \boldsymbol{v}_s - \boldsymbol{b}\right) = \operatorname{div}\left(\mathrm{D}_s \boldsymbol{S}_t\right), \tag{3-1}$$

EOM of motion of fluid phase:

$$\rho^f \mathrm{D}_f \boldsymbol{v}_f = -\gamma_w \operatorname{grad} h - \frac{\gamma_w}{k} n\left(\boldsymbol{v}_f - \boldsymbol{v}_s\right), \tag{3-2}$$

SWCE:

$$\operatorname{div} \boldsymbol{v}_s + \operatorname{div}\left\{n\left(\boldsymbol{v}_f - \boldsymbol{v}_s\right)\right\} = 0, \tag{3-3}$$

where $\rho_s = (1-n)\rho^s$ and $\rho_f = n\rho^f$ represent the solid and fluid phases densities, respectively (ρ^s: density of soil particles, ρ^f: density of pore water). D_s and D_f are the material-time derivatives with respect to the solid phase and fluid phase, respectively. $\boldsymbol{v}_s$ and $\boldsymbol{v}_f$ are the velocity vectors of the solid and fluid phases, respectively. $\mathrm{D}_s \boldsymbol{S}_t$ represents the nominal stress rate tensor of the mixture [20]. p denotes pore water pressure (compression is positive). h denotes total head and $\boldsymbol{b}$ is the body force vector per unit mass. n denotes the porosity. k is the permeability coefficient. γ_w represents the unit weight of water. The effect of taking the "rate-type" of the governing equation has been investigated in Section 4.2.

Conversely, consideration of the $\boldsymbol{u}$-p static seepage approximation, that is, the relative acceleration of pore water to the soil skeleton is negligibly smaller than the acceleration of the soil skeleton, expressed as:

$$\mathrm{D}_f \boldsymbol{v}_f - \mathrm{D}_s \boldsymbol{v}_s \ll \mathrm{D}_s \boldsymbol{v}_s. \tag{4}$$

Applying this expression in Equations (3-1 – 3-3) results in the following $\boldsymbol{u}$-p governing equation [5, 21]:

EOM of mixture (rate-type):

$$\rho \mathrm{D}_s^2 \boldsymbol{v}_s + \rho^f \left(\operatorname{div} \boldsymbol{v}_s\right)\left(\mathrm{D}_s \boldsymbol{v}_s - \boldsymbol{b}\right) = \operatorname{div}\left(\mathrm{D}_s \boldsymbol{S}_t\right), \tag{4-1}$$

SWCE:

$$\frac{\rho^f k}{\gamma_w} \operatorname{div}\left(\mathrm{D}_s \boldsymbol{v}_s\right) - \operatorname{div} \boldsymbol{v}_s + \operatorname{div}(k \operatorname{grad} h) = 0, \tag{4-2}$$

where $\rho = \rho_s + \rho_f = (1-n)\rho^s + n\rho^f$ is the mixture density. Note that $\mathrm{D}_s^2 \boldsymbol{v}_s$ is the third-order material-time derivative of displacement (i.e., the "jerk" term of the solid phase, [5]).

2.1.2 | Assumptions

To focus on the $\boldsymbol{u}$-p numerical instability, the following assumptions were introduced to eliminate other factors that could also cause instability:

- Linear elasticity: Material nonlinearity, such as material softening, which may induce instability, is neglected.
- Infinitesimal deformation: Geometrical nonlinearity, such as bifurcation-induced instability (e.g., buckling exhibiting peak strength), is neglected.

Furthermore, we assume:

- One-dimensional deformation/seepage: As discussed in the appendix of Toyoda and Noda [6], a one-dimensional evaluation is sufficient to address the multi-dimensional problem. By decomposing the $\boldsymbol{u}$-p governing equations into gradient terms (P-wave) and solenoidal terms (S-wave) using Helmholtz's theorem, the S-wave equation does not

10970207, 2025, 21, Downloaded from https://onlinelibrary.wiley.com/doi/10.1002/nme.70164 by Nagoya University, Wiley Online Library on [07/10/2026]. See the Terms and Conditions (https://onlinelibrary.wiley.com/terms-and-conditions) on Wiley Online Library for rules of use; OA articles are governed by the applicable Creative Commons License

include hydraulic pressure under the assumption of non-dilatant material. Therefore, "$\boldsymbol{u}$-p-induced" instability cannot occur in the S-wave equation. As a result, a multi-dimensional investigation is unnecessary for assessing $\boldsymbol{u}$-p instability, as stability evaluation of the one-dimensional P-wave equation is sufficient.

- Incompressibility of pure materials (i.e., soil particles and pore water) for simplicity: Densities are considered constant, and thus, porosity is also assumed to be constant, under the assumption of infinitesimal deformation.

2.1.3 | One-Dimensional Equations and Discretization

Referring to Toyoda and Noda [6], we assumed a saturated soil column and considered its one-dimensional linear elastic infinitesimal deformation. By treating the equilibrium state as $T \to \infty$ as a reference configuration, Equations (4-1–4-2) can be rewritten as

EOM of mixture:

$$\rho \ddot{u}_s = E_c \frac{\partial^2 \dot{u}_s}{\partial z^2} - \frac{\partial \dot{p}}{\partial z}, \quad 0 < z < H, \quad t > 0, \tag{5-1}$$

SWCE:

$$\frac{\rho^f k}{\gamma_w} \frac{\partial \ddot{u}_s}{\partial z} - \frac{\partial \dot{u}_s}{\partial z} + \frac{k}{\gamma_w} \frac{\partial^2 p}{\partial z^2} = 0, \quad 0 < z < H, \quad t > 0. \tag{5-2}$$

where the superscript dot $(\,)^{\cdot}$ denotes the time derivative operator $\partial/\partial t$, respectively. u_s and u_f denote displacements of the solid and fluid phases, respectively. H denotes the thickness of the soil column. The one-dimensional averaged relative flow rate w is expressed as:

$$w = n\left(\dot{u}_f - \dot{u}_s\right) = -k\frac{\partial h}{\partial z} - \frac{\rho^f k}{\gamma_w}\ddot{u}_s, \tag{6}$$

z and t denote the vertical position and time, respectively. $E_c = (1-\nu)E/\{(1+\nu)(1-2\nu)\}$ denotes the one-dimensional stiffness (E: Young's modulus, ν: Poisson's ratio). At the bottom of the column ($z = 0$), we assumed a fixed boundary condition. At the top of the column ($z = H$), we assumed a traction boundary condition considering the instantaneous load application.

Boundary conditions:

$$u_s(z = 0, t) = 0, \quad t > 0, \tag{7-1}$$

$$\frac{\partial u_s}{\partial z}(z = H, t) = -\frac{q}{E_c}, \quad t > 0. \tag{7-2}$$

where q is the load magnitude. For the hydraulic boundary conditions of pore water pressure, undrained conditions were imposed at the bottom and atmospheric conditions at the top.

Hydraulic boundary conditions:

$$\frac{\partial p}{\partial z}(z = 0, t) = 0, \quad t > 0 \tag{8-1}$$

$$p(z = H, t) = 0, \quad t > 0 \tag{8-2}$$

As for the initial conditions, we assumed a stationary state without deformation.

Initial conditions:

$$u_s(z, t = 0) = 0, \quad 0 < z < H \tag{9-1}$$

$$\dot{u}_s(z, t = 0) = 0, \quad 0 < z < H \tag{9-2}$$

10970207, 2025, 21, Downloaded from https://onlinelibrary.wiley.com/doi/10.1002/nme.70164 by Nagoya University, Wiley Online Library on [07/10/2026]. See the Terms and Conditions (https://onlinelibrary.wiley.com/terms-and-conditions) on Wiley Online Library for rules of use; OA articles are governed by the applicable Creative Commons License

2.1.4 | Non-Dimensionalization

Definition of the dimensionless variables are:

$$Z = \frac{z}{H}, \quad T = \frac{c_v t}{H^2} = \frac{kE_c t}{\gamma_w H^2}, \tag{10-1}$$

$$U_s = \frac{u_s}{\delta}, \quad U_f = \frac{u_f}{\delta}, \quad P = \frac{p}{q}, \tag{10-2}$$

where Z and T denotes the relative position and time factor, respectively; the solid and fluid phases' dimensionless displacements are denoted as U_s and U_f, respectively; the dimensionless pore water pressure is denoted as P. The governing equations, Equations (5-1 – 5-2), can be expressed as

EOM of mixture (rate-type):

$$\frac{\mathrm{e}\left(G_s + \mathrm{e}\right)}{1 + G_s \mathrm{e}} \overset{\circ\circ\circ}{U}_s - 4h^2 \frac{\partial^2 \mathring{U}_s}{\partial Z^2} + 4h^2 \frac{\partial \mathring{P}}{\partial Z} = 0, \quad 0 < Z < 1, \quad T > 0, \tag{11-1}$$

SWCE:

$$\frac{\mathrm{e}(1 + \mathrm{e})}{1 + G_s \mathrm{e}} \frac{\partial \overset{\circ\circ}{U}_s}{\partial Z} - 4h^2 \frac{\partial \mathring{U}_s}{\partial Z} + 4h^2 \frac{\partial^2 P}{\partial Z^2} = 0, \quad 0 < Z < 1. \tag{11-2}$$

The flow rate in the dimensionless form W can also be derived from Equation (6) as:

$$W = -\frac{\partial P}{\partial Z} - \frac{\left(G_s - 1\right)\mathrm{e}}{1 + G_s \mathrm{e}} \frac{1}{4h^2} \overset{\circ\circ}{U}_s. \tag{12}$$

The dimensionless forms of the initial and boundary conditions (Equations 7-1 – 9-2) can be obtained as:

Boundary conditions/hydraulic boundary conditions:

$$U_s(Z = 0, T) = 0, \quad T > 0, \tag{13-1}$$

$$\frac{\partial U_s}{\partial Z}(Z = 1, T) = -1, \quad T > 0, \tag{13-2}$$

$$\frac{\partial P}{\partial Z}(Z = 0, T) = 0, \quad T > 0, \tag{14-1}$$

$$P(Z = 1, T) = 0, \quad T > 0. \tag{14-2}$$

Initial conditions:

$$U_s(Z, T = 0) = 0, \quad 0 < Z < 1, \tag{15-1}$$

$$\frac{\partial U_s}{\partial T}(Z, T = 0) = 0, \quad 0 < Z < 1, \tag{15-2}$$

where

$$\text{Final settlement}: \delta = \frac{qH}{E_c}, \tag{16-1}$$

$$\text{Dimensionless factor}: \ h = \frac{c_p H}{2c_v} = \frac{\gamma_w H}{2k\sqrt{\rho' E_c}}, \tag{16-2}$$

10970207, 2025, 21, Downloaded from https://onlinelibrary.wiley.com/doi/10.1002/nme.70164 by Nagoya University, Wiley Online Library on [07/10/2026]. See the Terms and Conditions (https://onlinelibrary.wiley.com/terms-and-conditions) on Wiley Online Library for rules of use; OA articles are governed by the applicable Creative Commons License

$$\text{Undamped wave celerity}: \ c_p = \sqrt{\frac{E_c}{\rho'}}, \tag{16-3}$$

$$\text{Coefficient of consolidation}: \ c_v = \frac{kE_c}{\gamma_w}, \tag{16-4}$$

$$\text{Balanced density}: \ \rho' = \rho_s + \frac{\rho_f}{\mathrm{e}^2}, \quad \rho_s = (1-n)\rho^s, \quad \rho_f = n\rho^f, \tag{16-5}$$

$$\text{Specific gravity}: \ G_s = \frac{\rho^s}{\rho^f}, \tag{16-6}$$

$$\text{Void ratio}: \ \mathrm{e} = \frac{n}{1-n}, \tag{16-7}$$

where the superscript circle $(\,)^\circ$ represents the dimensionless time derivative $\partial/\partial T$. Note that the dimensionless factor h inversely proportional to k controls the solution. Also note that the balanced density ρ' in Equation (16-5) is different from the mixture density ρ appeared in Equations (4-1) and (5-1).

2.2 | Theoretical Solution

Toyoda and Noda [6] derived the one-dimensional solution by recognizing that the dimensionless $\boldsymbol{u}$-p governing equations (Equations 11-1 and 11-2) derive a damped wave equation:

$$\frac{(G_s-1)\mathrm{e}}{1+G_s\mathrm{e}}\frac{\partial^2 U_s}{\partial T^2} = 4h^2\frac{\partial^2 U_s}{\partial Z^2} - 4h^2\frac{\partial U_s}{\partial T}, \tag{17-1}$$

$$\Longleftrightarrow \frac{\partial^2 U_s}{\partial T^2} = 4h^{\#2}\frac{\partial^2 U_s}{\partial Z^2} - 4h^{\#2}\frac{\partial U_s}{\partial T}, \quad h^\# = h\sqrt{\frac{1+G_s\mathrm{e}}{(G_s-1)\mathrm{e}}}, \tag{17-2}$$

The dimensionless solutions for U_s and P can be expressed as a superposition of eigenmodes:

$$U_s(Z,T) = \sum_{n=1}^{\infty}\frac{2\cdot(-1)^{n+1}}{\beta_n^2}\sin(\beta_n Z)F_n^\#(T)\exp\left(-2h^{\#2}T\right) - Z, \tag{18-1}$$

$$P(Z,T) = \sum_{n=1}^{\infty}\frac{2\cdot(-1)^{n+1}}{\beta_n}\cos(\beta_n Z)G_n^\#(T)\exp\left(-2h^{\#2}T\right), \tag{18-2}$$

where

$$\beta_n = \frac{2n-1}{2}\pi, \tag{19-1}$$

$$F_n^\#(T) = \begin{cases} \cosh\left(2h^\# D_n^\# T\right) + \frac{h^\#}{D_n^\#}\sinh\left(2h^\# D_n^\# T\right) & \left(\beta_n < h^\#\right) \\ 1 + 2h^{\#2}T & \left(\beta_n = h^\#\right) \\ \cos\left(2h^\# D_n'^\# T\right) + \frac{h^\#}{D_n'^\#}\sin\left(2h^\# D_n'^\# T\right) & \left(\beta_n > h^\#\right) \end{cases}, \tag{19-2}$$

$$G_n^\#(T) = \begin{cases} P_I^\#\cosh\left(2h^\# D_n^\# T\right) + \frac{(2-P_I^\#)h^\#}{D_n^\#}\sinh\left(2h^\# D_n^\# T\right) & \left(\beta_n < h^\#\right) \\ P_I^\# + 2\left(2-P_I^\#\right)h^{\#2}T & \left(\beta_n = h^\#\right) \\ P_I^\#\cos\left(2h^\# D_n'^\# T\right) + \frac{(2-P_I^\#)h^\#}{D_n'^\#}\sin\left(2h^\# D_n'^\# T\right) & \left(\beta_n > h^\#\right) \end{cases}, \tag{19-3}$$

10970207, 2025, 21, Downloaded from https://onlinelibrary.wiley.com/doi/10.1002/nme.70164 by Nagoya University, Wiley Online Library on [07/10/2026]. See the Terms and Conditions (https://onlinelibrary.wiley.com/terms-and-conditions) on Wiley Online Library for rules of use; OA articles are governed by the applicable Creative Commons License

$$D_n^{\#} = \sqrt{h^{\#2} - \beta_n^2},\ D_n'^{\#} = \sqrt{\beta_n^2 - h^{\#2}}, \tag{19-4}$$

$$P_I^{\#} = -\frac{1+\mathrm{e}}{G_s - 1}. \tag{19-5}$$

The theoretical solutions, Equations (18-1) and (18-2), depend on the parameter h (or $h^{\#}$). Each eigenmode exhibits hyperbolic or trigonometric time development, corresponding to overdamped or underdamped oscillations, respectively. Notably, the theoretical solutions, Equations (18-1–18-2), unconditionally converge as $T \to \infty$ for any h (or $h^{\#}$). Thus, the divergence of the $\boldsymbol{u}$-p formulation discussed in the subsequent sections is not theoretical but purely numerical.

2.3 | Discretization

The methods of spatiotemporal discretization were conformed to Noda et al. [5].

2.3.1 | Spatial Discretization

Detailed derivations of the following discretized forms have been included in Appendix A: Detailed Derivation of Discretized Governing Equation With Concrete Forms of Matrices and Vectors.

2.3.1.1 | Weak Form of Dimensionless Rate-Type EOM. First, the derivation of the weak form of the dimensionless rate-type EOM (Equation 11-1) is presented based on the finite element method. By integrating Equation (11-1) over the entire domain $0 \le Z \le 1$ after multiplying it by a dimensionless arbitrary function $\delta V(Z,T)$ satisfying $\delta V(0,T) = 0$ as per according to the fixed boundary condition in Equation (13-1), we obtain the following equation using Gauss's divergence theorem:

$$\int_0^1 \frac{\mathrm{e}\left(G_s+\mathrm{e}\right)}{1+G_s\mathrm{e}} \delta V \overset{\circ\circ\circ}{U}_s dZ + \int_0^1 4h^2 \frac{\partial \delta V}{\partial Z}\frac{\partial \mathring{U}_s}{\partial Z} dZ - \int_0^1 4h^2 \frac{\partial \delta V}{\partial Z}\mathring{P} dZ = 0 \tag{20}$$

2.3.1.2 | Finite Element Discretization of Dimensionless Rate-Type EOM. The dimensionless solid phase displacement U_s is iso-parametrically discretized with linear interpolation using the finite element method, while the dimensionless pore water pressure P is defined at each element using the finite volume method. The entire domain $0 \le Z \le 1$ is divided into m finite elements of equal thickness $\Delta Z = 1/m$, as shown in Figure 1. The nodal coordinates are expressed as $Z^i = i\Delta Z$ $(i = 0, \cdots, m)$, the nodal dimensionless solid displacements $U_s^i(T)$ $(i = 0, \cdots, m)$, and the elemental dimensionless pressures $P^i(T)$ $(i = 1, \cdots, m)$. Considering the arbitrariness of δV and the fixed boundary conditions in Equation (13-1), the following simultaneous ordinary differential equation is obtained:

$$\frac{\mathrm{e}\left(G_s+\mathrm{e}\right)}{1+G_s\mathrm{e}}[\mathrm{M}]\left\{\overset{\circ\circ\circ}{U}_s^{\mathrm{N}}\right\} + 4h^2[\mathrm{K}]\left\{\mathring{U}_s^{\mathrm{N}}\right\} - 4h^2[\mathrm{L}]^{\mathrm{T}}\left\{\mathring{P}^{\mathrm{E}}\right\} = \{0\}, \tag{21}$$

where the global mass, stiffness, and displacement-volume change converter matrices are denoted as [M], [K], and [L], respectively, $\left\{U_s^{\mathrm{N}}\right\}$ and $\left\{P^{\mathrm{E}}\right\}$ are the global coefficient vectors listing $U_s^i(T)$ and $P^i(T)$, respectively. The transpose operator of a matrix is denoted as the superscript "T", and the zero vector is denoted as $\{0\}$. A detailed derivation of Equation (21), along with the specific forms of the matrices, is included in Appendix A: Derivation of Discretized Dimensionless Rate-Type EOM.

2.3.1.3 | Physical Model of Dimensionless Physical Model of Seepage. Regarding the discretization of the dimensionless SWCE (Equation 11-2), we refer to the physical model of seepage presented by Asaoka et al. [22], derived from Christian [23] and Akai and Tamura [24]. The detailed formulation of the model and the discretization of the diffusion term, that is, the third term of Equation (11-2), are provided in Appendix A: Formulation of Dimensionless Physical Model of Seepage.

10970207, 2025, 21, Downloaded from https://onlinelibrary.wiley.com/doi/10.1002/nme.70164 by Nagoya University, Wiley Online Library on [07/10/2026]. See the Terms and Conditions (https://onlinelibrary.wiley.com/terms-and-conditions) on Wiley Online Library for rules of use; OA articles are governed by the applicable Creative Commons License

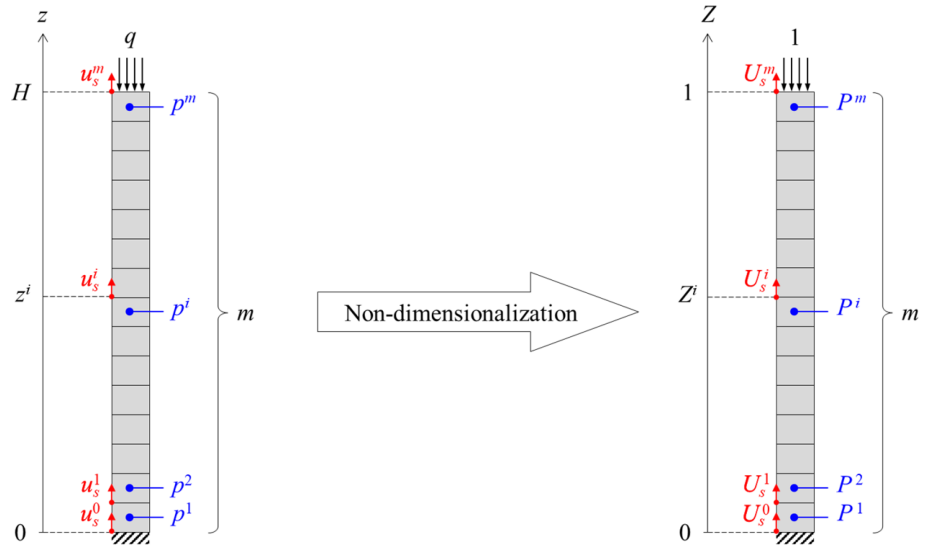


FIGURE 1 | One-dimensional finite element/finite volume modelling.

2.3.1.4 | Finite Volume Discretization of Dimensionless SWCE. Taking the weak form of the dimensionless SWCE by the finite volume method, the spatial integration of Equation (11-2) within each element $Z^{(1)} \le Z \le Z^{(2)}$ is expressed as:

$$\int_{Z^{(1)}}^{Z^{(2)}} \frac{\mathrm{e}(1+\mathrm{e})}{1+G_s\mathrm{e}} \frac{\partial \overset{\circ\circ}{U}_s}{\partial Z} dZ - \int_{Z^{(1)}}^{Z^{(2)}} 4h^2 \frac{\partial \overset{\circ}{U}_s}{\partial Z} dZ + \int_{Z^{(1)}}^{Z^{(2)}} 4h^2 \frac{\partial^2 P}{\partial Z^2} dZ = 0. \tag{22}$$

Discretizing Equation (22), we obtain:

$$\frac{\mathrm{e}(1+\mathrm{e})}{1+G_s\mathrm{e}}[\mathrm{L}]\left\{\overset{\circ\circ\mathrm{N}}{U_s}\right\} - 4h^2[\mathrm{L}]\left\{\overset{\circ\mathrm{N}}{U_s}\right\} + 4h^2[\mathrm{H}]\left\{P^{\mathrm{E}}\right\} = 0 \tag{23}$$

where the derivation is included in Appendix A: Derivation of Discretized Dimensionless SWCE. Here, [H] represents the discretized Laplacian operator matrix.

2.3.2 | Time Integration Formula and Simultaneous Recursive Equation

In this paper, we primarily employed *Wilson-θ*, a well-known implicit time integration formula for dynamic problems, to derive the simultaneous recursive equation for time integration. Additionally, *Newmark-β* is discussed in Section 4.3.

Following Noda et al. [5], we assume linear transience of the "jerk" term of the solid phase $\overset{\circ\circ\circ}{U}_s$ (the third dimensionless time derivative of dimensionless solid displacement), within the dimensionless time interval $T = T$ to $T = T + \theta\Delta T$ (θ: parameter of *Wilson-θ*, introduced in [14]) at all nodes:

Linearity of the dimensionless jerk term:

$$\left\{\overset{\circ\circ\circ\mathrm{N}}{U_s}\right\}\Big|_{T+\tau} = \left\{\overset{\circ\circ\circ\mathrm{N}}{U_s}\right\}\Big|_{T} + \frac{\tau}{\theta\Delta T}\left(\left\{\overset{\circ\circ\circ\mathrm{N}}{U_s}\right\}\Big|_{T+\theta\Delta T} - \left\{\overset{\circ\circ\circ\mathrm{N}}{U_s}\right\}\Big|_{T}\right),\ 0 \le \tau \le \theta\Delta T. \tag{24}$$

Integrating Equation (24) with respect to τ, we obtain the time integration formula by substituting $\tau = \theta\Delta T$:

$$\left\{(\theta\Delta T)^2\overset{\circ\circ\mathrm{N}}{U_s}\right\}\Big|_{T+\theta\Delta T} = \left\{(\theta\Delta T)^2\overset{\circ\circ\mathrm{N}}{U_s}\right\}\Big|_{T} + \frac{1}{2}\left\{(\theta\Delta T)^3\overset{\circ\circ\circ\mathrm{N}}{U_s}\right\}\Big|_{T} + \frac{1}{2}\left\{(\theta\Delta T)^3\overset{\circ\circ\circ\mathrm{N}}{U_s}\right\}\Big|_{T+\theta\Delta T}, \tag{25-1}$$

$$\left\{(\theta\Delta T)\overset{\circ\mathrm{N}}{U_s}\right\}\Big|_{T+\theta\Delta T} = \left\{(\theta\Delta T)\overset{\circ\mathrm{N}}{U_s}\right\}\Big|_{T} + \left\{(\theta\Delta T)^2\overset{\circ\circ\mathrm{N}}{U_s}\right\}\Big|_{T} + \frac{1}{3}\left\{(\theta\Delta T)^3\overset{\circ\circ\circ\mathrm{N}}{U_s}\right\}\Big|_{T} + \frac{1}{6}\left\{(\theta\Delta T)^3\overset{\circ\circ\circ\mathrm{N}}{U_s}\right\}\Big|_{T+\theta\Delta T}, \tag{25-2}$$

10970207, 2025, 21, Downloaded from https://onlinelibrary.wiley.com/doi/10.1002/nme.70164 by Nagoya University, Wiley Online Library on [07/10/2026]. See the Terms and Conditions (https://onlinelibrary.wiley.com/terms-and-conditions) on Wiley Online Library for rules of use; OA articles are governed by the applicable Creative Commons License

For estimating variables at the next step $T = T + \Delta T$, we substitute $\tau = \Delta T$:

$$\left\{(\theta\Delta T)^3 \overset{\circ\circ\circ}{U}{}^{\mathrm{N}}_s\right\}\Big|_{T+\Delta T} = \left(1-\frac{1}{\theta}\right)\left\{(\theta\Delta T)^3 \overset{\circ\circ\circ}{U}{}^{\mathrm{N}}_s\right\}\Big|_{T} + \frac{1}{\theta}\left\{(\theta\Delta T)^3 \overset{\circ\circ\circ}{U}{}^{\mathrm{N}}_s\right\}\Big|_{T+\theta\Delta T}, \tag{26-1}$$

$$\left\{(\theta\Delta T)^2 \overset{\circ\circ}{U}{}^{\mathrm{N}}_s\right\}\Big|_{T+\Delta T} = \left\{(\theta\Delta T)^2 \overset{\circ\circ}{U}{}^{\mathrm{N}}_s\right\}\Big|_{T} + \left(\frac{1}{\theta}-\frac{1}{2\theta^2}\right)\left\{(\theta\Delta T)^3 \overset{\circ\circ\circ}{U}{}^{\mathrm{N}}_s\right\}\Big|_{T} + \frac{1}{2\theta^2}\left\{(\theta\Delta T)^3 \overset{\circ\circ\circ}{U}{}^{\mathrm{N}}_s\right\}\Big|_{T+\theta\Delta T}, \tag{26-2}$$

$$\left\{(\theta\Delta T)\mathring{U}{}^{\mathrm{N}}_s\right\}\Big|_{T+\Delta T} = \left\{(\theta\Delta T)\mathring{U}{}^{\mathrm{N}}_s\right\}\Big|_{T} + \frac{1}{\theta}\left\{(\theta\Delta T)^2 \overset{\circ\circ}{U}{}^{\mathrm{N}}_s\right\}\Big|_{T} + \left(\frac{1}{2\theta^2}-\frac{1}{6\theta^3}\right)\left\{(\theta\Delta T)^3 \overset{\circ\circ\circ}{U}{}^{\mathrm{N}}_s\right\}\Big|_{T} + \frac{1}{6\theta^3}\left\{(\theta\Delta T)^3 \overset{\circ\circ\circ}{U}{}^{\mathrm{N}}_s\right\}\Big|_{T+\theta\Delta T}. \tag{26-3}$$

Using the trapezoidal rule for dimensionless pore water pressure P, assuming linearity of its rate for all elements, we obtain:

$$\left\{P^{\mathrm{E}}\right\}\Big|_{T+\theta\Delta T} = \left\{P^{\mathrm{E}}\right\}\Big|_{T} + \frac{1}{2}\left(\left\{(\theta\Delta T)\mathring{P}^{\mathrm{E}}\right\}\Big|_{T} + \left\{(\theta\Delta T)\mathring{P}^{\mathrm{E}}\right\}\Big|_{T+\theta\Delta T}\right), \tag{27}$$

$$\left\{(\theta\Delta T)\mathring{P}^{\mathrm{E}}\right\}\Big|_{T+\Delta T} = \left(1-\frac{1}{\theta}\right)\left\{(\theta\Delta T)\mathring{P}^{\mathrm{E}}\right\}\Big|_{T} + \frac{1}{\theta}\left\{(\theta\Delta T)\mathring{P}^{\mathrm{E}}\right\}\Big|_{T+\theta\Delta T}, \tag{28-1}$$

$$\left\{P^{\mathrm{E}}\right\}\Big|_{T+\Delta T} = \left\{P^{\mathrm{E}}\right\}\Big|_{T} + \left(\frac{1}{\theta}-\frac{1}{2\theta^2}\right)\left\{(\theta\Delta T)\mathring{P}^{\mathrm{E}}\right\}\Big|_{T} + \frac{1}{2\theta^2}\left\{(\theta\Delta T)\mathring{P}^{\mathrm{E}}\right\}\Big|_{T+\theta\Delta T}. \tag{28-2}$$

Note that setting $\theta > 1.37$ exhibits unconditional convergence for second-order linear ordinary differential equations [25].

Assuming Equations (21) and (23) are satisfied at $T = T + \theta\Delta T$, with Equations (25-1), (25-2), and (27), we obtain:

$$\mathrm{A}\boldsymbol{u}_{n+\theta} = \mathrm{B}\boldsymbol{u}_n \tag{29-1}$$

The equation for estimating the states at $T = T + \Delta T$ (at the next $(n+1)$-th step) is

$$\boldsymbol{u}_{n+1} = \mathrm{C}\boldsymbol{u}_n + \mathrm{D}\boldsymbol{u}_{n+\theta}, \tag{29-2}$$

where $\boldsymbol{u}_n$, $\boldsymbol{u}_{n+1}$, and $\boldsymbol{u}_{n+\theta}$ are listing vectors of the state variables at $T = T$, $T + \theta\Delta T$, and $T + \Delta T$, respectively.

$$\boldsymbol{u}_n = \begin{bmatrix} \left\{(\theta\Delta T)^3 \overset{\circ\circ\circ}{U}{}^{\mathrm{N}}_s\right\}\Big|_{T} \\ \left\{(\theta\Delta T)^2 \overset{\circ\circ}{U}{}^{\mathrm{N}}_s\right\}\Big|_{T} \\ \left\{(\theta\Delta T)\mathring{U}{}^{\mathrm{N}}_s\right\}\Big|_{T} \\ \left\{(\theta\Delta T)\mathring{P}^{\mathrm{E}}\right\}\Big|_{T} \\ \left\{P^{\mathrm{E}}\right\}\Big|_{T} \end{bmatrix}, \boldsymbol{u}_{n+1} = \begin{bmatrix} \left\{(\theta\Delta T)^3 \overset{\circ\circ\circ}{U}{}^{\mathrm{N}}_s\right\}\Big|_{T+\Delta T} \\ \left\{(\theta\Delta T)^2 \overset{\circ\circ}{U}{}^{\mathrm{N}}_s\right\}\Big|_{T+\Delta T} \\ \left\{(\theta\Delta T)\mathring{U}{}^{\mathrm{N}}_s\right\}\Big|_{T+\Delta T} \\ \left\{(\theta\Delta T)\mathring{P}^{\mathrm{E}}\right\}\Big|_{T+\Delta T} \\ \left\{P^{\mathrm{E}}\right\}\Big|_{T+\Delta T} \end{bmatrix}, \boldsymbol{u}_{n+\theta} = \begin{bmatrix} \left\{(\theta\Delta T)^3 \overset{\circ\circ\circ}{U}{}^{\mathrm{N}}_s\right\}\Big|_{T+\theta\Delta T} \\ \left\{(\theta\Delta T)^2 \overset{\circ\circ}{U}{}^{\mathrm{N}}_s\right\}\Big|_{T+\theta\Delta T} \\ \left\{(\theta\Delta T)\mathring{U}{}^{\mathrm{N}}_s\right\}\Big|_{T+\theta\Delta T} \\ \left\{(\theta\Delta T)\mathring{P}^{\mathrm{E}}\right\}\Big|_{T+\theta\Delta T} \\ \left\{P^{\mathrm{E}}\right\}\Big|_{T+\theta\Delta T} \end{bmatrix}, \tag{30}$$

The concrete forms of the coefficient matrices A, B, C, and D are summarized in Appendix A: Specific Form of Matrices in Simultaneous Recursive Equations. By eliminating $\boldsymbol{u}_{n+\theta}$ from Equations (29-1–29-2), we obtain the simultaneous recursive equation:

$$\boldsymbol{u}_{n+1} = \mathrm{E}\boldsymbol{u}_n, \mathrm{E} = \mathrm{C} + \mathrm{D}\mathrm{A}^{-1}\mathrm{B}, \tag{31}$$

where E is a real nonsymmetric diagonalizable coefficient matrix.

10970207, 2025, 21, Downloaded from https://onlinelibrary.wiley.com/doi/10.1002/nme.70164 by Nagoya University, Wiley Online Library on [07/10/2026]. See the Terms and Conditions (https://onlinelibrary.wiley.com/terms-and-conditions) on Wiley Online Library for rules of use; OA articles are governed by the applicable Creative Commons License

2.3.3 | $\gamma_{\theta 1}$ Criterion

Assuming SWCE (Equation (23)) is satisfied at $T = T + \theta\Delta T$ and utilizing the formulas of *Wilson-θ* (Equations (25-1) and (25-2)):

$$-\gamma_{\theta 1}[\mathrm{L}]\left\{(\theta\Delta T)^3 \overset{\circ\circ\circ}{U}{}_s^{\mathrm{N}}\right\}\Big|_{T+\theta\Delta T} + (\theta\Delta T)[\mathrm{H}]\left\{P^{\mathrm{E}}\right\}\Big|_{T+\theta\Delta T} = [\mathrm{L}]\left\{(\theta\Delta T)\mathring{U}_s^{\mathrm{N}}\right\}\Big|_T + \gamma_{\theta 2}[\mathrm{L}]\left\{(\theta\Delta T)^2 \overset{\circ\circ}{U}{}_s^{\mathrm{N}}\right\}\Big|_T + \gamma_{\theta 3}[\mathrm{L}]\left\{(\theta\Delta T)^3 \overset{\circ\circ\circ}{U}{}_s^{\mathrm{N}}\right\}\Big|_T, \tag{32}$$

where

$$\gamma_{\theta 1} = \frac{1}{6} - \frac{1}{2\theta\Delta T}\frac{1}{4h^2}\frac{\mathrm{e}(1+\mathrm{e})}{1+G_s\mathrm{e}}, \gamma_{\theta 2} = 1 - \frac{1}{\theta\Delta T}\frac{1}{4h^2}\frac{\mathrm{e}(1+\mathrm{e})}{1+G_s\mathrm{e}}, \gamma_{\theta 3} = \frac{1}{6}\left(2 - \frac{3}{\theta\Delta T}\frac{1}{4h^2}\frac{\mathrm{e}(1+\mathrm{e})}{1+G_s\mathrm{e}}\right), \tag{33}$$

where $\Delta T = c_v\Delta t/H^2$ denotes the dimensionless time increment. If $\gamma_{\theta 1}$ becomes negative due to high permeability (small dimensionless factor h) or high temporal discretization resolution (small ΔT), sign inversion occurs in the first term of the left-hand side of Equation (32), leading to the divergence of excess pore water pressure (i.e., a negative coefficient of consolidation, consistent with Terzaghi's static theory of consolidation). According to Noda et al. [5], this phenomenon appears to trigger illogical behavior in the $\boldsymbol{u}$-p formulation (e.g., pore water absorption/drainage coupled with volumetric expansion/compression of the soil skeleton). Notably, the lower limit of Δt increases with a larger coefficient of permeability k, making calculations in high-frequency ranges (which require smaller Δt for accuracy) more challenging.

Rewriting the dimensionless expression of $\gamma_{\theta 1}$ from Equation (33) in dimensional form using Equations (16-2–16-7), we obtain:

$$\gamma_{\theta 1} = \frac{1}{6} - \frac{1}{2\theta\Delta t}\frac{\rho^f k}{\gamma_w} \tag{34}$$

The above equation is the same as Equation (1), indicating that the ratio $k/\Delta t$ controls the possibility of $\boldsymbol{u}$-p calculations. Note that the specific form of $\gamma_{\theta 1}$ changes when assuming linearity of higher/lower-order derivatives of U_s, or using alternative time integration methods (e.g., *Newmark-β*).

2.3.4 | Procedure of Direct Numerical Stability Evaluation Using Spectral Radius

The eigenvalue problem for the matrix E in the simultaneous recursive equation (Equation 31) is defined as:

$$\mathrm{E}\boldsymbol{p}_i = \lambda_i\boldsymbol{p}_i, \mathrm{E} = \mathrm{P}^{-1}\Lambda\mathrm{P}, \tag{35}$$

where $\Lambda = \mathrm{diag}\left(\lambda_1, \lambda_2, \cdots, \lambda_N\right)$ is the diagonal matrix of E, whose components λ_i $(i = 1, \cdots, N)$ are the eigenvalues of E, $\mathrm{P} = \left[\boldsymbol{p}_1, \boldsymbol{p}_2, \cdots, \boldsymbol{p}_N\right]$ is the matrix of eigenvectors $\boldsymbol{p}_i$ $(i = 1, \cdots, N)$, N is the size of E. The eigenvectors $\left(\boldsymbol{p}_1, \boldsymbol{p}_2, \cdots, \boldsymbol{p}_N\right)$ are normalized by their respective 2-norm (i.e., $\left\|\boldsymbol{p}_i\right\| = 1$, $i = 1, \cdots, N$, $\|\ \|$: the 2-norm vector-to-scalar operator) and sorted in descending order of the magnitude of eigenvalues $\left(\left|\lambda_1\right|, \left|\lambda_2\right|, \cdots, \left|\lambda_N\right|\right)$, where $|\ |$ denotes the absolute value operator of scalars.

For the simultaneous recursive equation (Equation 31), the explicit formula for $\boldsymbol{u}_n$ can be expressed using the initial state vector $\boldsymbol{u}_0$ as follows:

$$\boldsymbol{u}_n = \mathrm{E}^n\boldsymbol{u}_0, \mathrm{E}^n = \mathrm{P}^{-1}\Lambda^n\mathrm{P}, \tag{36}$$

Decomposing the initial state vector in the direction of eigenvectors as $\boldsymbol{u}_0 = \boldsymbol{b}_1 + \boldsymbol{b}_2 + \cdots + \boldsymbol{b}_N$ (i.e., direct sum of eigenvectors; $\boldsymbol{b}_k$: is a component of $\boldsymbol{u}_0$ in the direction of eigenvector $\boldsymbol{p}_k$, $k = 1, 2, \cdots, N$), $\boldsymbol{u}_n$ can be expressed as a superposition of eigenvectors multiplied by eigenvalues during time integration as:

$$\boldsymbol{u}_n = \lambda_1^n\boldsymbol{b}_1 + \lambda_2^n\boldsymbol{b}_2 + \cdots + \lambda_N^n\boldsymbol{b}_N. \tag{37}$$

Thus, the convergence of $\boldsymbol{u}_n$ at $n \to \infty$ is ensured for any initial value $\boldsymbol{u}_0$ if the magnitude of all eigenvalues $\left|\lambda_i\right|$ $(i = 1, 2, \cdots, N)$ is less than 1. Defining the spectral radius $\rho(\mathrm{E})$ as:

$$\rho(\mathrm{E}) = \max\left(\left|\lambda_1\right|, \left|\lambda_2\right|, \cdots, \left|\lambda_N\right|\right), \tag{38}$$

10970207, 2025, 21, Downloaded from https://onlinelibrary.wiley.com/doi/10.1002/nme.70164 by Nagoya University, Wiley Online Library on [07/10/2026]. See the Terms and Conditions (https://onlinelibrary.wiley.com/terms-and-conditions) on Wiley Online Library for rules of use; OA articles are governed by the applicable Creative Commons License

The convergence condition for the simultaneous recursive equation (Equation 31) can be expressed as:

$$\rho(\mathrm{E}) \leq 1 \ldots \text{Stable.} \tag{39}$$

Equation (39) represents the stability criterion based on the spectral radius.

3 | Analysis Results

3.1 | Preliminary Study

Through the single-phase analysis following Bathe and Wilson [14], as detailed in Appendix A: Single-Phase Stability Analysis, the validity of the proposed stability analysis has been confirmed, including the reliability of the solver used for eigenvalue analysis.

3.2 | Investigation on Stable Range of *u-p*

To explore the stable range of the ***u***-*p* formulation, the spectral radius of the matrix E in Equation (31) was calculated by varying the permeability coefficient k and the time increment Δt using *Wilson-θ*. The number of elements was set to $m = 10$, which was deemed sufficient for convergence with respect to mesh refinement, as preliminary analyses by the authors confirmed that further increasing the number of elements did not affect the spectral radius. Typical parameter values were used: Young's modulus $E = 10^4$ kPa, Poisson's ratio $\nu = 0.30$, thickness $H = 1$ m, specific gravity $G_s = 2.65$, void ratio $\mathrm{e} = 1.0$, and the parameter $\theta = 1.40$ for *Wilson-θ*, which ensures unconditional convergence for a single-phase linear system. The effects of these parameters are discussed in Section 4.1. For the eigenvalue analysis of the matrix E, the nonsymmetric eigenvalue problem solver from LAPACK (Intel Math Kernel Library) was employed.

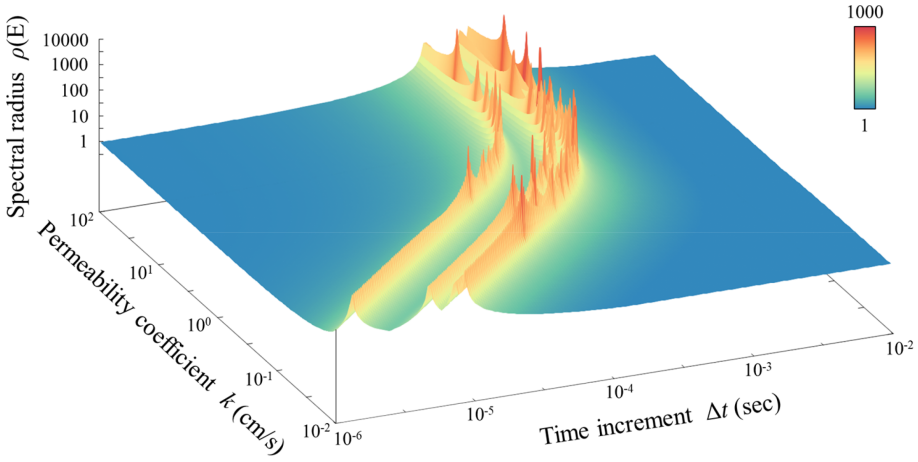
Figure 2a shows the distribution of the spectral radius $\rho(\mathrm{E})$ with respect to the permeability coefficient k and the time increment Δt. A mountain chain-shaped distribution of $\rho(\mathrm{E})$ is observed. By binarizing $\rho(\mathrm{E})$ with the threshold value $1.0 + \delta$ (δ: a sufficiently small value, e.g., 10^{-4}), the stable/unstable region of ***u***-*p* in the $k - \Delta t$ space is illustrated in Figure 3. The green region in Figure 3 indicates the stable region of ***u***-*p* ($\rho(\mathrm{E}) \leq 1$), while the pale green region indicates the unstable region ($\rho(\mathrm{E}) > 1$).

As shown in Figure 3, the band-shaped unstable region of ***u***-*p* ($\rho(\mathrm{E}) > 1$, henceforth referred to as the "unstable band") is clearly observed. Characteristically, the unstable band bends at the center of the figure; it distributes diagonally in the lower region (low-permeability range) and vertically in the upper region (high-permeability range).

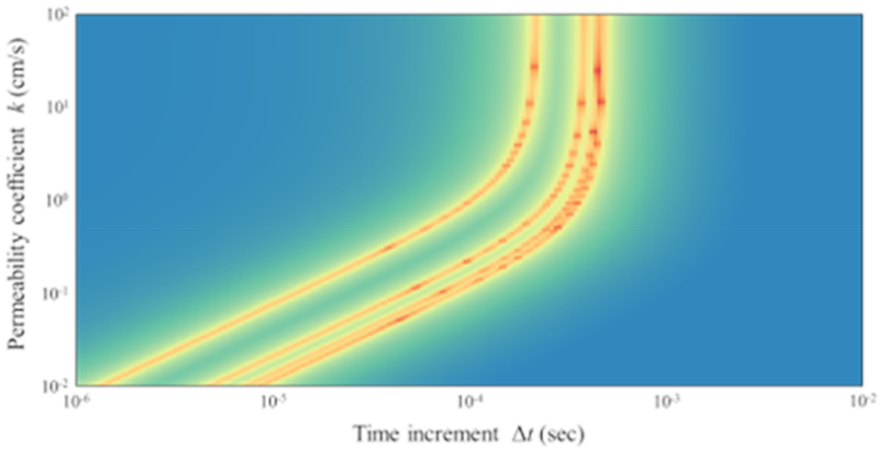
- In region (I), located in the low-permeability range of Figure 3, the ***u***-*p* calculation becomes unstable when the ratio of the permeability coefficient to the time increment $k/\Delta t$ exceeds a certain threshold. The red threshold line in Figure 3 represents the $\gamma_{\theta 1}$ criterion proposed by Noda et al. [5], where the lower and upper regions correspond to the applicable and inapplicable ranges of ***u***-*p*, as estimated by the criterion. Comparing this criterion with the boundary line between the stable and unstable regions, determined through stability analysis, shows that the judgment based on the criterion is moderately effective in the low-permeability range.
- In region (II), located in the high-permeability range of Figure 3, the possibility of ***u***-*p* calculations depends entirely on the time increment Δt. In this region, the $\gamma_{\theta 1}$ criterion is completely inconsistent with the results of stability analysis. However, notably, stable calculations do not necessarily correspond to accurate solutions for dynamic soil-water coupling simulations. A larger Δt compromises accuracy, while a smaller Δt leads to numerical divergence (i.e., a limitation of ***u***-*p*). Furthermore, even if the numerical solution matches the theoretical ***u***-*p* solution, it may deviate from the *Full* solution (***u***-***w***-*p*) due to the neglect of the relative acceleration of the fluid phase [4, 6].
- In region (III), located above the unstable band, $\rho(\mathrm{E}) \simeq 1$ because there is almost no stepwise deformation due to an extremely small time increment $\Delta t < 10^{-8}$ s. This means a large number of calculation steps is required to capture the targeted phenomena. Moreover, even if the calculation is stable, the correspondence of the ***u***-*p* solution to the *Full* solution is not guaranteed due to the high permeability [6]. Thus, this region is considered substantially inapplicable for ***u***-*p* and is excluded from further discussion in the following sections.

Next, let us discuss why the threshold between the stable and unstable ranges of ***u***-*p* bends at a certain permeability coefficient. As mentioned in Section 2.2, the one-dimensional theoretical solution of ***u***-*p* is expressed as the superposition of

10970207, 2025, 21, Downloaded from https://onlinelibrary.wiley.com/doi/10.1002/nme.70164 by Nagoya University, Wiley Online Library on [07/10/2026]. See the Terms and Conditions (https://onlinelibrary.wiley.com/terms-and-conditions) on Wiley Online Library for rules of use; OA articles are governed by the applicable Creative Commons License



(a) Distribution of spectral radius



(b) Contour of spectral radius

FIGURE 2 | Spectral radius distribution on $k-\Delta t$ space.

eigenmodes in Equations (18-1) and (18-2), where each eigenmode exhibits either overdamped or underdamped oscillation depending on the permeability coefficient k. Figure 4 illustrates the theoretical solution of $\boldsymbol{u}$-p with respect to k. When the solution includes at least one mode exhibiting overdamping ($\beta_1 < h^{\#}$; $k < 3.2$ cm/s), it demonstrates quasi-static consolidation. Conversely, when all eigenmodes exhibit underdamping ($\beta_1 > h^{\#}$; $k > 3.2$ cm/s), the solution demonstrates damped oscillation. Notably, the theoretical solution is independent of the time increment Δt. Additionally, the $\beta_n = h^{\#}$ line in Figure 3 represents the condition of critical damping for the n-th mode ($n = 1, 2, \cdots$), that is, where the n-th mode exhibits overdamped or underdamped oscillation below or above the threshold line, respectively. Specifically, the $\beta_1 = h^{\#}$ line in Figure 3, which delineates whether the theoretical solution exhibits static consolidation or damped oscillation, aligns with the bend in the threshold. Thus, we hypothesize that the bending of the threshold is caused by changes in the diverging eigenmodes due to the transition of the theoretical solution between static consolidation and damped oscillation.

3.3 | Investigation on Eigenmodes of Simultaneous Recursive Equation

3.3.1 | Stable Region

Before focusing on the diverging eigenmodes, the eigenvalues and eigenmodes within the stable region were preliminarily investigated. At point A ($k = 10^{-5}$ cm/s, $\Delta t = 10^{-3}$ s) in Figure 3, located in the stable region (I) beneath the $\beta_1 = h^{\#}$ threshold exhibiting static consolidation, the magnitudes of the 1st–50th eigenvalues $|\lambda_i|$ ($i = 1, \cdots, 50$) are listed in

10970207, 2025, 21, Downloaded from https://onlinelibrary.wiley.com/doi/10.1002/nme.70164 by Nagoya University, Wiley Online Library on [07/10/2026]. See the Terms and Conditions (https://onlinelibrary.wiley.com/terms-and-conditions) on Wiley Online Library for rules of use; OA articles are governed by the applicable Creative Commons License

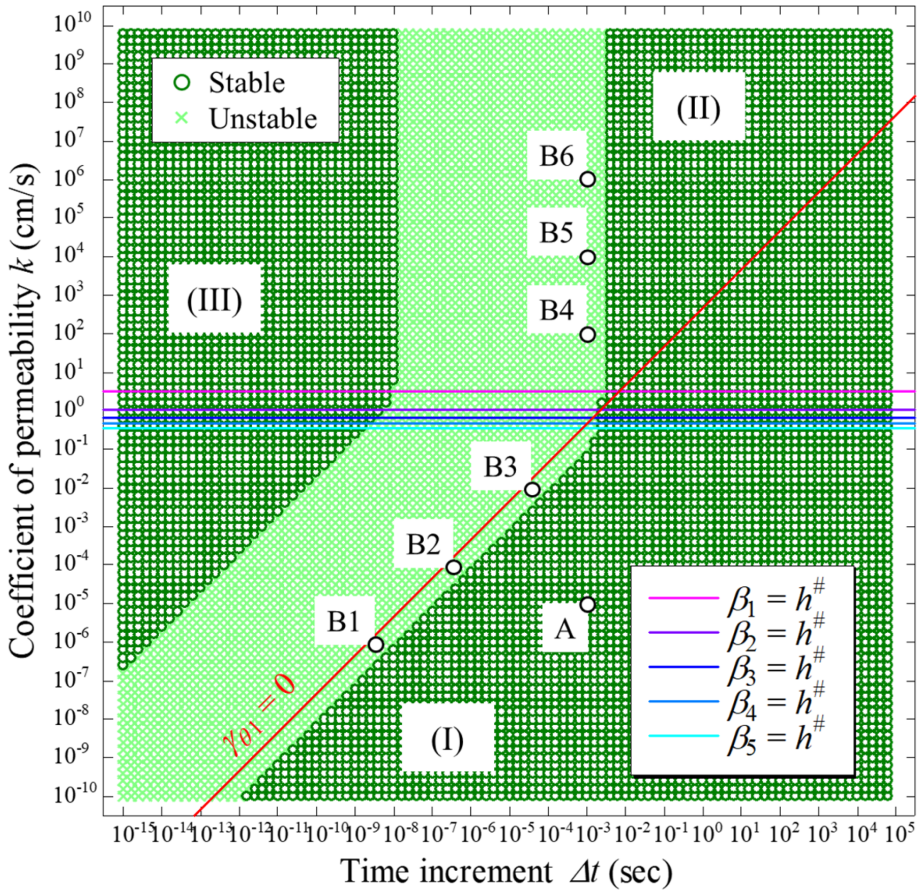


FIGURE 3 | Stable/unstable range of $\boldsymbol{u}$-p on $k-\Delta t$ space.

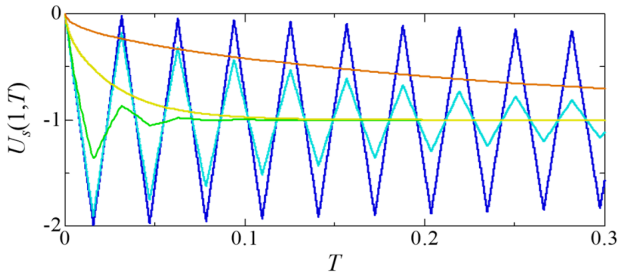
Figure 5. The absence of eigenvalues exceeding 1 (i.e., $\rho(\mathrm{E}) \leq 1$), ensures the convergence of the solution as $T \to \infty$. Additionally, the convergence speed of each mode is governed by the magnitude of the eigenvalue $|\lambda_i|$. Modes with smaller eigenvalue magnitudes rapidly converge to zero, while modes with larger eigenvalue magnitudes closer to 1 persist during the progression of time steps. For example, while the 11th mode (eigenvalue: $\lambda_{11} = 0.778$) requires only 10 updates to dissipate 90% of its original vector magnitude, the 1st mode (eigenvalue: $\lambda_1 = 0.999999662$) requires approximately 6.8 million updates to achieve the same degree of dissipation.

To understand the significant difference in convergence speed between the 11th and 1st modes, we compared the eigenvectors of the 11th and 1st modes $\boldsymbol{p}_{11}$ and $\boldsymbol{p}_1$. Figure 6 illustrates the 50 components of the eigenvectors $\boldsymbol{p}_{11}$ and $\boldsymbol{p}_1$, representing the directions of these eigenvectors in a 50-dimensional space. Additionally, the correspondence of each component of an eigenvector to a nodal or elemental variable is summarized in Table 1, based on the definition of the state vector in Equation (30).

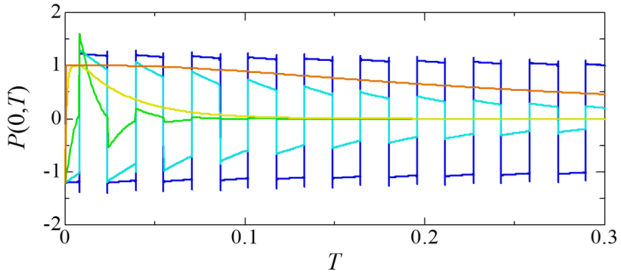
The eigenvector of the 11th mode $\boldsymbol{p}_{11}$, shown in Figure 6a, contains significant magnitudes of the dimensionless acceleration $(\theta\Delta T)^2\overset{\circ\circ}{U}_s$ along with other derivative terms ($(\theta\Delta T)^3\overset{\circ\circ\circ}{U}_s$, $(\theta\Delta T)\mathring{U}_s$, and $(\theta\Delta T)\mathring{P}$). In contrast, the eigenvector of the 1st mode $\boldsymbol{p}_1$, shown in Figure 6b, prominently features the dimensionless pore water pressure P while exhibiting negligibly small magnitudes for $(\theta\Delta T)^2\overset{\circ\circ}{U}_s$. Therefore, the 11th mode, with its small eigenvalue magnitude leading to rapid convergence, corresponds to dynamic deformation, whereas the 1st mode, with an eigenvalue magnitude near 1 and persisting over time, corresponds to static consolidation.

The same discussion can also be applied to the other eigenmodes. In Figure 5, the degree of dynamics was evaluated using the spatially maximum magnitude of the dimensionless acceleration $\left|(\theta\Delta T)^2\overset{\circ\circ}{U}_s\right|_{\max}$ as an index expressing the prominence of acceleration components in the respective eigenmodes. The 12th–50th eigenmodes, which have small eigenvalue magnitudes and exhibit rapid convergence, are also dynamic modes containing significant

10970207, 2025, 21, Downloaded from https://onlinelibrary.wiley.com/doi/10.1002/nme.70164 by Nagoya University, Wiley Online Library on [07/10/2026]. See the Terms and Conditions (https://onlinelibrary.wiley.com/terms-and-conditions) on Wiley Online Library for rules of use; OA articles are governed by the applicable Creative Commons License



(a) Dimensionless displacement at top normalized by final settlement $U_s(1,T)$ – dimensionless time T relation



(b) Dimensionless pore water pressure at bottom normalized by vertical load $P(0,T)$ – dimensionless time T relation

Coefficient of permeability k (cm/s)	Graph	Mode number n						
		1	2	3	…	15	16	…
10^3		UD	UD	UD	…	UD	UD	…
10^2		UD	UD	UD	…	UD	UD	…
10^1		UD	UD	UD	…	UD	UD	…
10^0		OD	UD	UD	…	UD	UD	…
10^{-1}		OD	OD	OD	…	OD	UD	…

- UD: The mode exhibits underdamping ($\beta_n < h^{\#}$)
- OD: The mode exhibits overdamping ($\beta_n > h^{\#}$)

FIGURE 4 | Theoretical solution of ***u***-p (instantaneous load application).

magnitudes of acceleration in their eigenvectors, as shown in Figure 5. Conversely, the 2nd–10th modes and the 1st mode exhibit relatively negligible nodal acceleration magnitudes ($(\theta\Delta T)^2\ddot{U}_s < 10^{-9}$), indicating static consolidation. Furthermore, we confirmed that the 1st–10th static eigenmodes correspond to the modes of Terzaghi's static consolidation:

- Comparing the eigenvalues of the 1st–10th eigenmodes shown in Figure 7, the lower-order modes have greater eigenvalue magnitudes than the higher-order modes, meaning that higher-order modes exhibit faster convergence.
- The distribution of dimensionless pressure P (i.e., the 41st–50th components of an eigenvector), shown in Figure 8, aligns with the behavior of the modes in Terzaghi's theory of consolidation.

Hence, the convergence of the solution progresses in the following order: (1) dynamic modes, (2) higher-order static modes, and (3) lower-order static modes. Notably, the persistent lower-order modes have larger eigenvalues in the simultaneous recursive equation, whereas the eigenvalues of these modes in Terzaghi's static consolidation equation are comparatively small. Additionally, we confirmed that all eigenvalues are real and positive, ensuring that the time development of the solution at any position exhibits a monotonic exponential decrease.

3.3.2 | Unstable Region

To understand the characteristics of numerical divergence in the unstable region ($\rho(\mathrm{E}) > 1$) shown in Figure 3, we investigated the behavior of the diverging eigenmodes. Six points along the unstable band were selected: B1–B3 in the

10970207, 2025, 21, Downloaded from https://onlinelibrary.wiley.com/doi/10.1002/nme.70164 by Nagoya University, Wiley Online Library on [07/10/2026]. See the Terms and Conditions (https://onlinelibrary.wiley.com/terms-and-conditions) on Wiley Online Library for rules of use; OA articles are governed by the applicable Creative Commons License

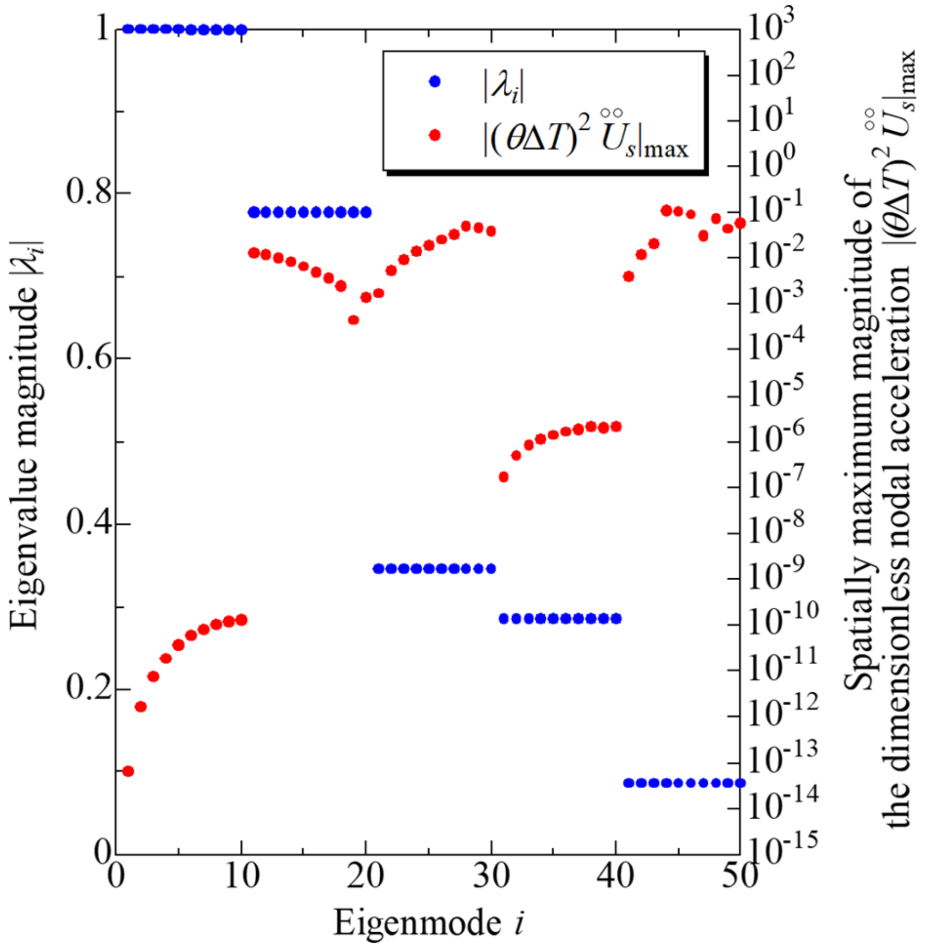


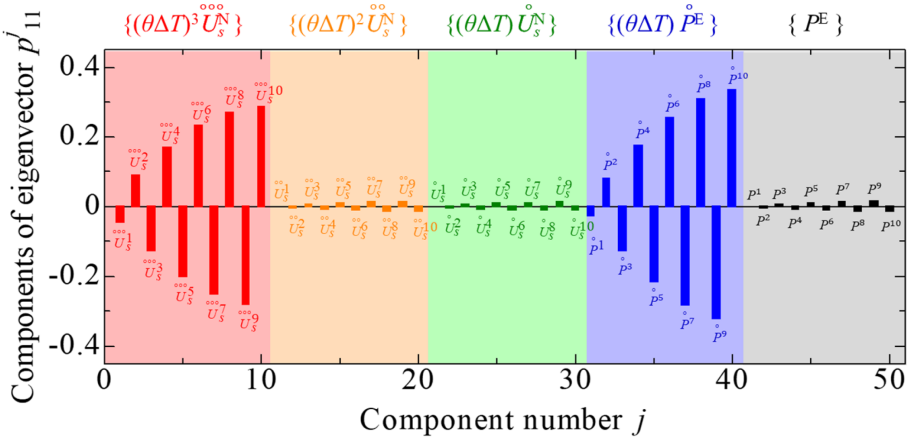
FIGURE 5 | Magnitude of eigenvalues $|\lambda_i|$ and spatially maximum magnitude of dimensionless nodal acceleration $\left|(\theta\Delta T)^2 \overset{\circ\circ}{U}_s\right|_{\max} = \max_{j=11,\cdots,20}\left(\left|p_i^j\right|\right)$ of i-th eigenmode. * p_i^j: j-th component of eigenvector i-th eigenmode defined as $p_i^j = \boldsymbol{p}_i \cdot \boldsymbol{e}_j$ $(j = 1, \cdots, 50)$. * $\boldsymbol{e}_j$: unit vector orthogonal basis vector in 50th dimensional space satisfying $\boldsymbol{e}_j \cdot \boldsymbol{e}_k = \delta_{jk}$ $(k = 1, \cdots, 50)$.

low-permeability range and B4–B6 in the high-permeability range. Focusing on the diverging eigenmode with the largest eigenvalue magnitude (i.e., the 1st mode, henceforth referred to as "the most unstable eigenmode"), the conditions and eigenvalues of the most unstable eigenmode λ_1 at points B1–B6 are summarized in Table 2. The eigenvector components of the most unstable eigenmode $\boldsymbol{p}_1$ are shown in Figure 9.

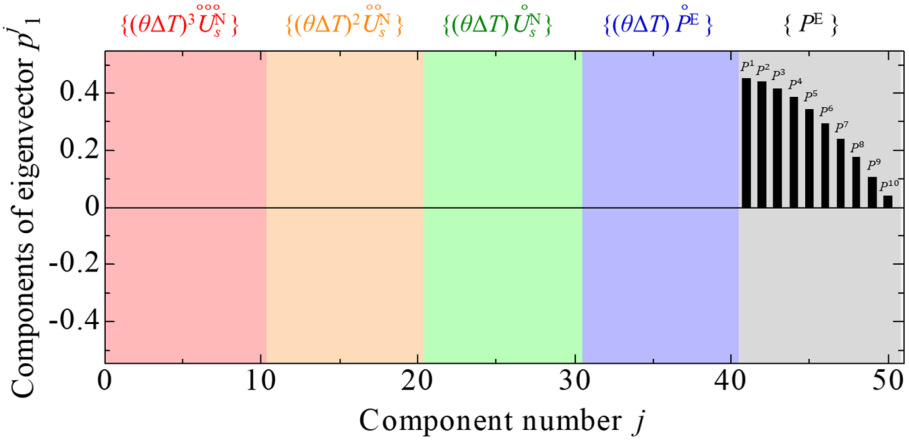
3.3.2.1 | Common Features of Most Unstable Eigenmodes Between Low and Highly Permeable Ranges. As shown in Table 2, the eigenvalues of the most unstable eigenmode are all real and negative. This indicates that the sign of the components of the initial state vector along $\boldsymbol{p}_1$ alternates with each state update, while the amplitude increases (similar to oscillating divergence in a geometric progression). Regarding the dimensionless pore water pressure distribution (41st–50th components in Figure 9), pressures in adjacent elements exhibit opposite signs (i.e., a checkerboard pattern of pore water pressure in the color map). These features—oscillating divergence in the time history and the checkerboard-pattern pressure distribution—are indicative of numerical instability in ***u***-*p* calculations.

3.3.2.2 | Different Features of Most Unstable Eigenmodes Between Low and Highly Permeable Ranges. Referring to Table 2, the eigenvalues of the 1st mode λ_1 at B1–B3 with the same $k/\Delta t$ are identical, indicating that the eigenvalue depends solely on $k/\Delta t$ in the low-permeability range. Additionally, the corresponding eigenvectors $\boldsymbol{p}_1$ at B1–B3 are parallel in the 50-dimensional space (i.e., the matrix E is coaxial). Thus, the characteristics of the diverging eigenmode are consistent in the low-permeability range. Conversely, λ_1 at B4–B6 with the same Δt are also identical, indicating that the eigenvalue depends only on Δt in the high-permeability range. Similarly, the parallelism of $\boldsymbol{p}_1$ among B4–B6 suggests a unique diverging eigenmode in the high-permeability range.

10970207, 2025, 21, Downloaded from https://onlinelibrary.wiley.com/doi/10.1002/nme.70164 by Nagoya University, Wiley Online Library on [07/10/2026]. See the Terms and Conditions (https://onlinelibrary.wiley.com/terms-and-conditions) on Wiley Online Library for rules of use; OA articles are governed by the applicable Creative Commons License



(a) 11th mode $\boldsymbol{p}_{11}$



(b) 1st mode $\boldsymbol{p}_1$

FIGURE 6 | Components of eigenvectors.

However, the directions of $\boldsymbol{p}_1$ at B1–B3 and B4–B6 in the 50-dimensional space are entirely different. As shown in Figure 9, eigenvectors at B1–B3 in the low-permeability range predominantly feature pressure-related components ($(\theta\Delta T)\mathring{P}$: 31st–40th, P: 41st–50th components), with negligible displacement-related components ($(\theta\Delta T)^3\overset{\circ\circ\circ}{U}_s$: 1st–10th, $(\theta\Delta T)^2\overset{\circ\circ}{U}_s$: 11th–20th, $(\theta\Delta T)\mathring{U}_s$: 21st–30th components), thereby indicating that numerical divergence in the low-permeability range is driven by the magnification of the checkerboard pressure distribution, with minimal deformation of the solid phase. In contrast, eigenvectors at B4–B6 in the high-permeability range include significant deformation-related components, leading to numerical divergence in both displacement and pressure.

The difference between the eigenvectors at B1–B3 and B4–B6 appears to be caused by the switching of the dominant eigenmode at the bend in the unstable region. While this initially suggests that different eigenmodes diverge in the low- and high-permeability ranges, Figure 2b reveals smooth transitions in eigenvalues rather than abrupt changes. This suggests that the eigenvector undergoes a gradual rotation near the bend, driven by changes in the components of matrix E as k and Δt vary along the unstable band.

3.3.2.3 | Nature of Illogical Phenomenon in Unstable Region of *u-p*. To investigate the illogical phenomena violating the SWCE (mass conservation law of saturated soil) observed in the unstable range of ***u-p*** calculations, we examined the relationships among the distributions of the dimensionless volumetric strain rate $\mathring{\varepsilon}$, its derivatives (defined in

10970207, 2025, 21, Downloaded from https://onlinelibrary.wiley.com/doi/10.1002/nme.70164 by Nagoya University, Wiley Online Library on [07/10/2026]. See the Terms and Conditions (https://onlinelibrary.wiley.com/terms-and-conditions) on Wiley Online Library for rules of use; OA articles are governed by the applicable Creative Commons License

TABLE 1 | Correspondence of eigenvector components.

Component	Variable		
1	Dimensionless **nodal jerk** of solid phase	Node 1	$(\theta\Delta T)^3\mathring{U}_s^1$
2		Node 2	$(\theta\Delta T)^3\mathring{U}_s^2$
⋮		⋮	⋮
10		Node 10	$(\theta\Delta T)^3\mathring{U}_s^{10}$
11	Dimensionless **nodal acceleration** of solid phase	Node 1	$(\theta\Delta T)^2\mathring{U}_s^1$
12		Node 2	$(\theta\Delta T)^2\mathring{U}_s^2$
⋮		⋮	⋮
20		Node 10	$(\theta\Delta T)^2\mathring{U}_s^{10}$
21	Dimensionless **nodal velocity** of solid phase	Node 1	$(\theta\Delta T)\mathring{U}_s^1$
22		Node 2	$(\theta\Delta T)\mathring{U}_s^2$
⋮		⋮	⋮
30		Node 10	$(\theta\Delta T)\mathring{U}_s^{10}$
31	Dimensionless **elemental pore water pressure rate**	Element 1	$(\theta\Delta T)\mathring{P}^1$
32		Element 2	$(\theta\Delta T)\mathring{P}^2$
⋮		⋮	⋮
40		Element 10	$(\theta\Delta T)\mathring{P}^{10}$
41	Dimensionless **elemental pore water pressure rate**	Element 1	P^1
42		Element 2	P^2
⋮		⋮	⋮
50		Element 10	P^{10}

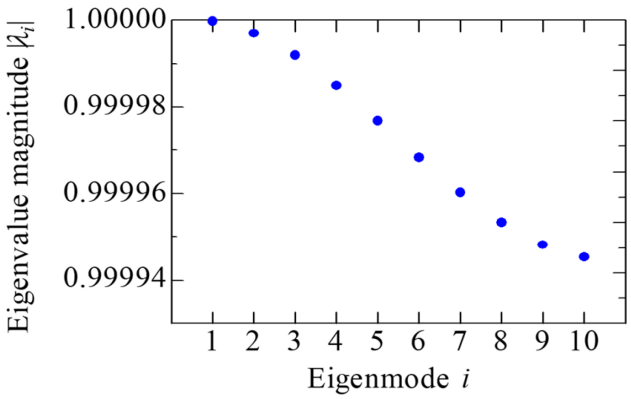


FIGURE 7 | Eigenvalues of 1st—10th eigenmodes (magnified Figure 5 at green-boxed area).

Equation A20-2), and dimensionless pressure P for the most unstable eigenmode in Figure 10. Cases B2 and B5 were selected as representative points in the low- and high-permeability ranges, respectively.

The signs of the dimensionless volumetric strain rate $\mathring{\varepsilon}$ and dimensionless pressure P were found to be identical at each element for both B2 and B5, indicating no violation of SWCE. However, the higher-order derivatives of the volumetric strain $\mathring{\mathring{\varepsilon}}$ and $\mathring{\mathring{\mathring{\varepsilon}}}$ exhibited opposite signs to P at each element for both B2 and B5, which might intuitively seem illogical.

10970207, 2025, 21, Downloaded from https://onlinelibrary.wiley.com/doi/10.1002/nme.70164 by Nagoya University, Wiley Online Library on [07/10/2026]. See the Terms and Conditions (https://onlinelibrary.wiley.com/terms-and-conditions) on Wiley Online Library for rules of use; OA articles are governed by the applicable Creative Commons License

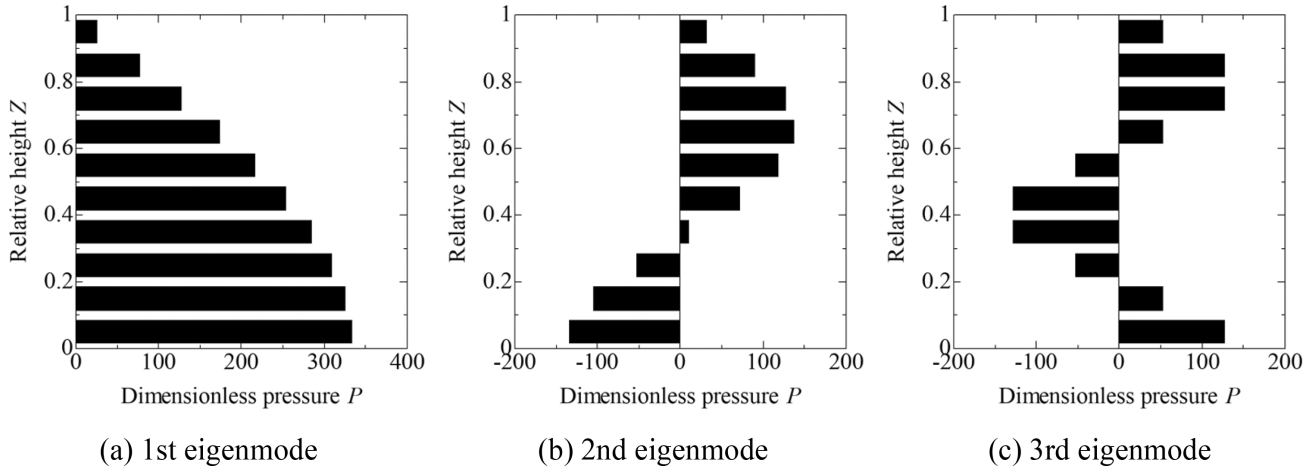


FIGURE 8 | Distribution of dimensionless pore water pressure P.

TABLE 2 | Conditions and results of eigenvalue analysis at Points B1—B6.

	Permeability coefficient k (cm/s)	Time increment (s)	$k/\Delta t$ (cm/s^2)	Eigenvalue λ_1 (maximum magnitude)
B1	$10^{-6.0}$	$10^{-8.5}$	$10^{2.5}$	−1.69
B2	$10^{-4.0}$	$10^{-6.5}$	$10^{2.5}$	−1.69
B3	$10^{-2.0}$	$10^{-4.5}$	$10^{2.5}$	−1.69
B4	$10^{2.0}$	$10^{-3.0}$	$10^{5.0}$	−2.09
B5	$10^{4.0}$	$10^{-3.0}$	$10^{7.0}$	−2.09
B6	$10^{6.0}$	$10^{-3.0}$	$10^{9.0}$	−2.09

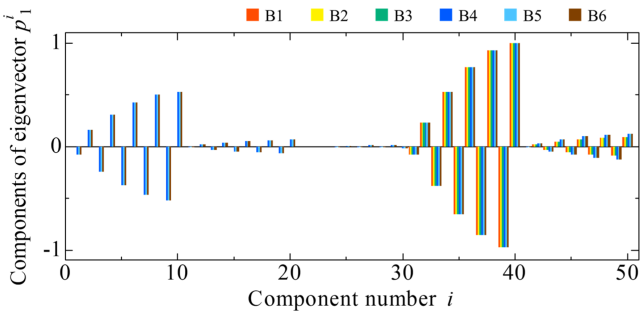


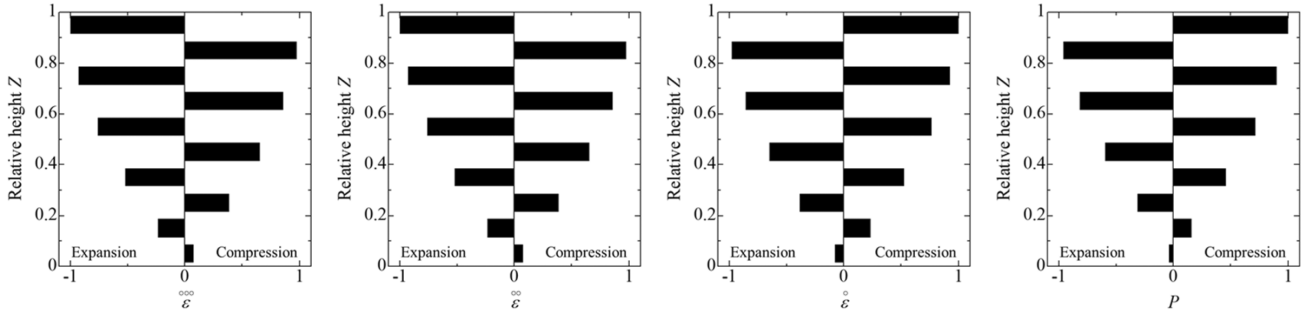
FIGURE 9 | Components of eigenvectors* of diverging eigenmodes with maximum magnitude of eigenvalue. * Normalized so that maximum magnitude of components is 1.

Noda et al. [5] noted that the left-hand side of the discretized SWCE (including inertial terms, Equation 32) is isomorphic to that of the static SWCE and derived the $\gamma_{\theta 1}$ criterion based on the physical meaning of SWCE. However, the intuitively derived $\gamma_{\theta 1}$ criterion provided just the "rough estimation" for judging instability, not ensured the strict satisfaction of SWCE. The confusion of higher-order derivatives with the first-order derivative of displacement or volumetric strain in the derivation of the $\gamma_{\theta 1}$ criterion could lead to misconceptions that SWCE is violated, even though SWCE is indeed satisfied as part of the governing equations.

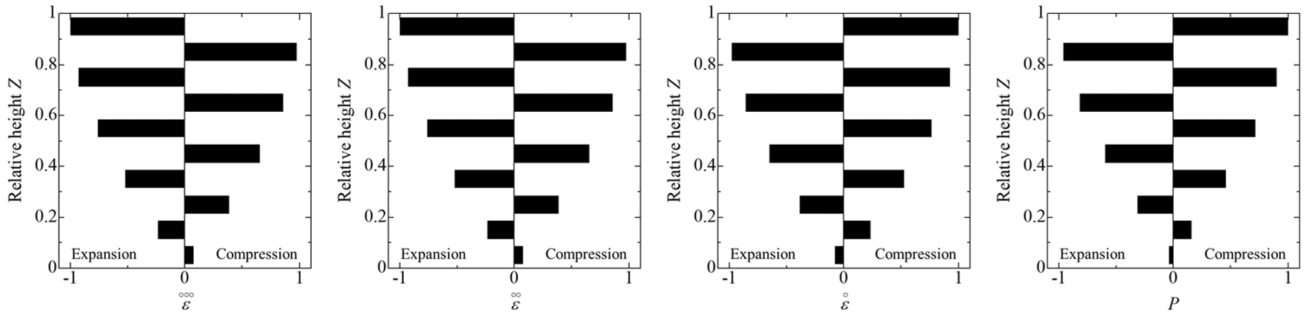
4 | Supplementary Discussions

In this section, investigations into the factors affecting the distribution of the unstable region are provided.

10970207, 2025, 21, Downloaded from https://onlinelibrary.wiley.com/doi/10.1002/nme.70164 by Nagoya University, Wiley Online Library on [07/10/2026]. See the Terms and Conditions (https://onlinelibrary.wiley.com/terms-and-conditions) on Wiley Online Library for rules of use; OA articles are governed by the applicable Creative Commons License



(a) Point B2 (low permeable range)



(a) Point B5 (highly permeable range)

FIGURE 10 | Comparison of dimensionless volumetric strain rate*, its derivatives*, and dimensionless pressure* of diverging eigenmodes with maximum magnitude of eigenvalue. * Normalized so that the maximum magnitude of each variable is 1.

4.1 | Parametric Studies

4.1.1 | Effects of Young's Modulus E, Poisson's Ratio ν, and Thickness H

Young's modulus E and Poisson's ratio ν affect the one-dimensional stiffness $E_c = (1-\nu)E/\{(1+\nu)(1-2\nu)\}$, which corresponds to the reciprocal of the coefficient of volume compressibility m_v. Considering the definition of the dimensionless factor h in Equation (16-2) and the dimensionless time increment $\Delta T = \left(c_v/H^2\right)\Delta t = \left(kE_c/\gamma_w H^2\right)\Delta t$ (c.f. Equation (10-1)) that constitutes the recursive matrix E in Equation (31), multiplying H by 0.1 or E_c by 100 is equivalent to multiplying both k and Δt by 100 in terms of the components of the matrix E. Thus, the unstable band shifts parallelly to the $\gamma_{\theta 1}$ criterion, as shown in Figures 11 and 12. Notably, the threshold in the low-permeability range is independent of E, ν, and H, thereby confirming the validity of the $\gamma_{\theta 1}$ criterion, independent of E, ν, and H in the low-permeability range.

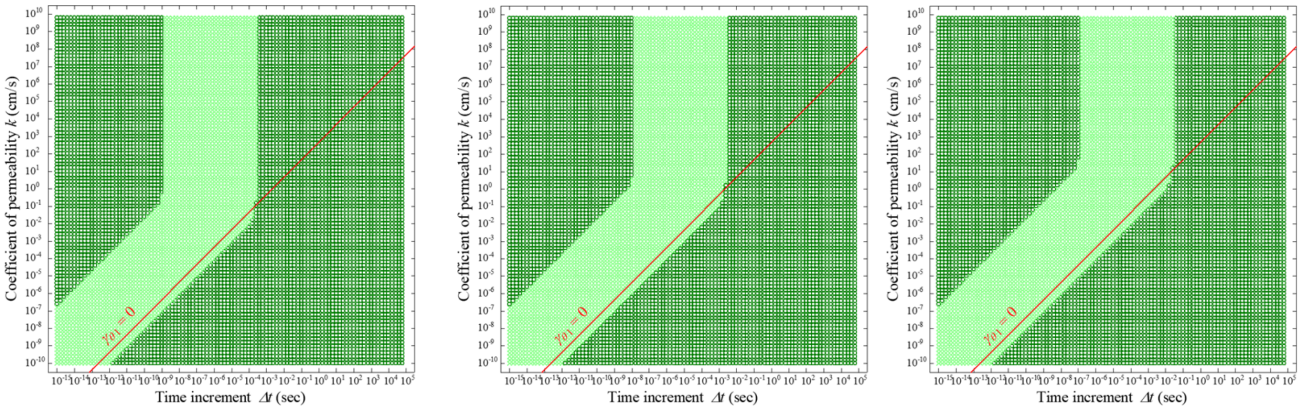
4.1.2 | Effects of Specific Gravity G_s, Void Ratio e

Specific gravity G_s and void ratio e have no significant effect on the unstable band. As shown in Figures 13 and 14, greater values of G_s and e tend to narrow the unstable band.

4.1.3 | Effect of Parameter θ

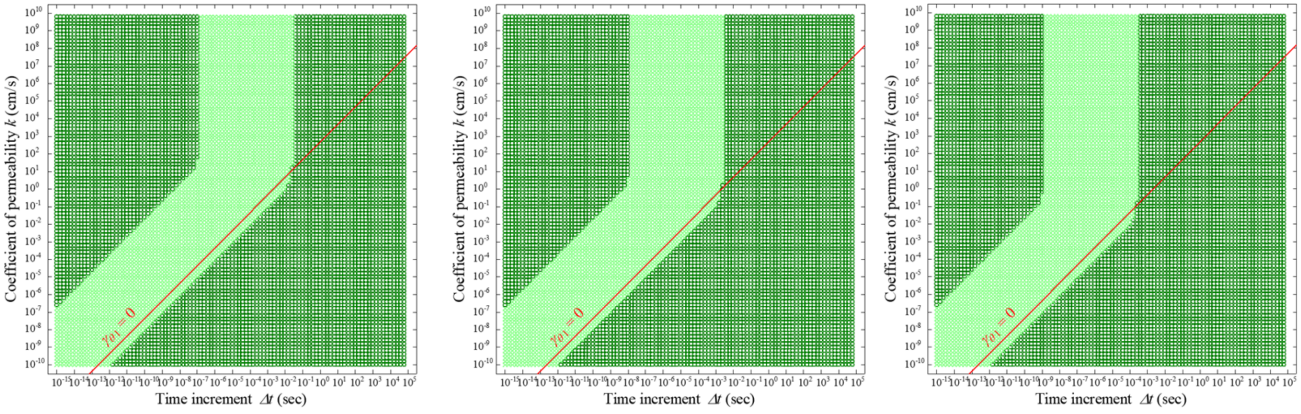
Bathe and Wilson [14] derived the criterion $\theta > 1.37$ to ensure unconditional convergence for the linear system of single-phase materials. The stable region for the two-phase $\boldsymbol{u}$-p cases in this study also varies with θ, as shown in Figure 15. When $\theta < 1.37$, as depicted in Figure 15a,b, the stable region is eliminated, except for region (III) in Figure 3. Therefore, the criterion $\theta > 1.37$ remains valid as a prerequisite for the stability of two-phase systems.

10970207, 2025, 21, Downloaded from https://onlinelibrary.wiley.com/doi/10.1002/nme.70164 by Nagoya University, Wiley Online Library on [07/10/2026]. See the Terms and Conditions (https://onlinelibrary.wiley.com/terms-and-conditions) on Wiley Online Library for rules of use; OA articles are governed by the applicable Creative Commons License



(a) $E = 10^2$ kPa (b) $E = 10^4$ kPa (c) $E = 10^6$ kPa

FIGURE 11 | Effect of Young's modulus (= 0.30, = 1 m, = 2.65, = 1.0, = 1.40).



(a) $H = 0.1$ m (b) $H = 1$ m (c) $H = 10$ m

FIGURE 12 | Effect of thickness (= 10^4 kPa, = 0.30, = 2.65, = 1.0, = 1.40).

4.2 | Effects of Taking Rate-Type of Governing Equations and Order of Time Integration Formula

In this section, we investigate the effects of adopting the rate-type governing equations and the order of the time integration formula. Table 3 presents four combinations, Cases [1]–[4], of governing equations and the assumed linearity of the time-integration formula. The governing equations and time-integration formula not used in the earlier sections are defined as:

EOM of mixture:

$$\frac{\mathrm{e}\left(G_s+\mathrm{e}\right)}{1+G_s\mathrm{e}}\overset{\circ\circ}{U}_s-4h^2\frac{\partial^2 U_s}{\partial Z^2}+4h^2\frac{\partial P}{\partial Z}=0,\quad 0<Z<1,\quad t>0, \tag{40}$$

SWCE (Rate-type):

$$\frac{\mathrm{e}(1+\mathrm{e})}{1+G_s\mathrm{e}}\frac{\partial\overset{\circ\circ\circ}{U}_s}{\partial Z}-4h^2\frac{\partial\overset{\circ\circ}{U}_s}{\partial Z}+4h^2\frac{\partial^2\mathring{P}}{\partial Z^2}=0,\quad 0<Z<1. \tag{41}$$

Linearity of the dimensionless acceleration term:

$$\left\{\overset{\circ\circ\mathrm{N}}{U}_s\right\}\Big|_{T+\tau}=\left\{\overset{\circ\circ\mathrm{N}}{U}_s\right\}\Big|_{T}+\frac{\tau}{\theta\Delta T}\left(\left\{\overset{\circ\circ\mathrm{N}}{U}_s\right\}\Big|_{T+\theta\Delta T}-\left\{\overset{\circ\circ\mathrm{N}}{U}_s\right\}\Big|_{T}\right),\quad 0\le\tau\le\theta\Delta T. \tag{42}$$

10970207, 2025, 21, Downloaded from https://onlinelibrary.wiley.com/doi/10.1002/nme.70164 by Nagoya University, Wiley Online Library on [07/10/2026]. See the Terms and Conditions (https://onlinelibrary.wiley.com/terms-and-conditions) on Wiley Online Library for rules of use; OA articles are governed by the applicable Creative Commons License

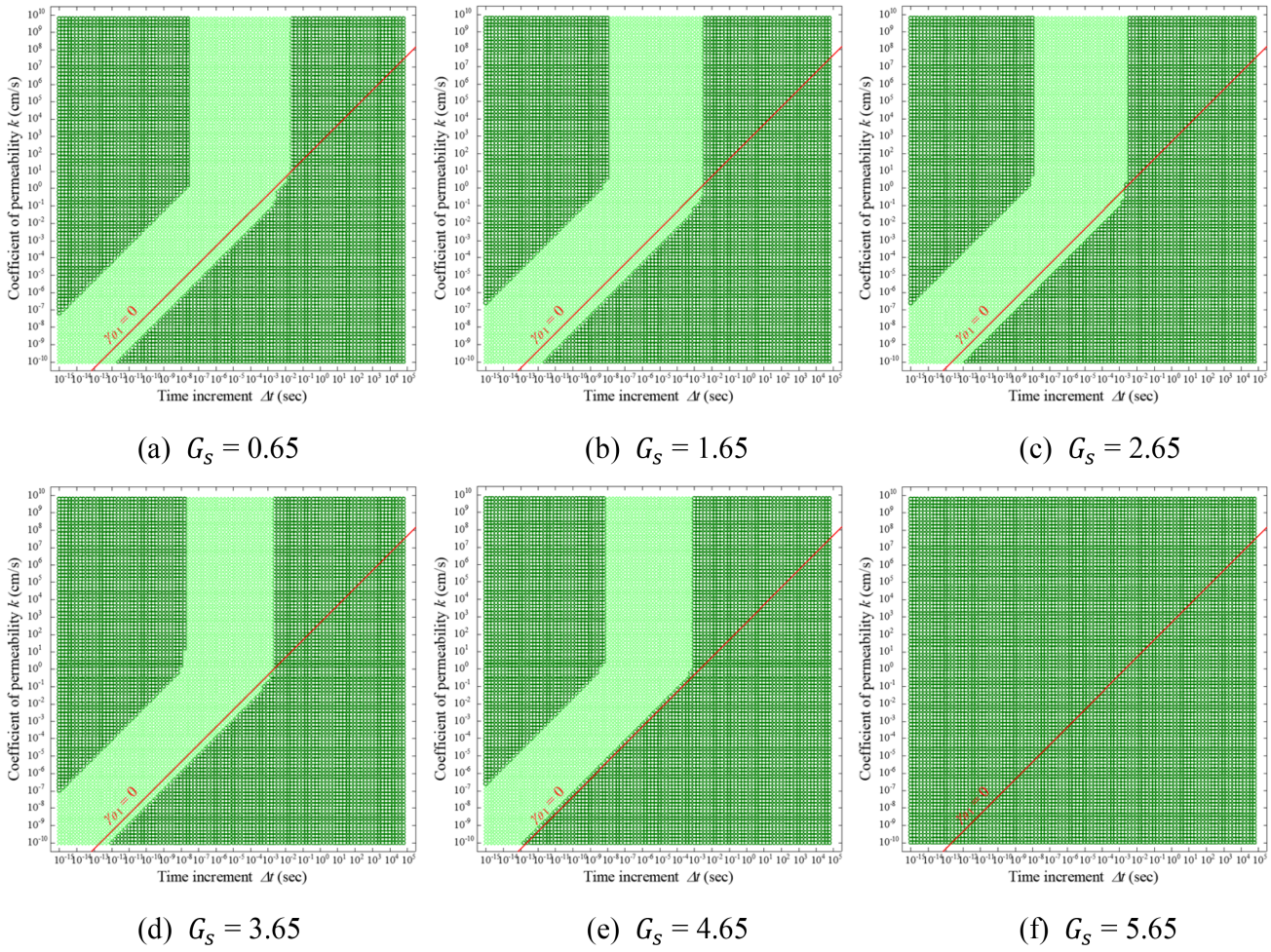


FIGURE 13 | Effect of specific gravity (= 10^4 kPa, = 0.30, = 1 m, = 1.0, = 1.40).

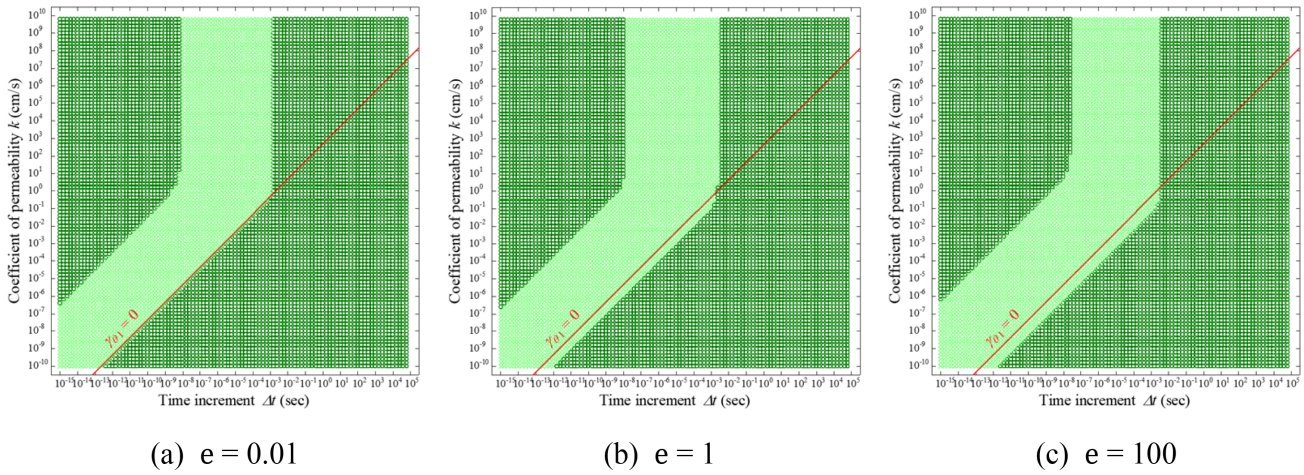


FIGURE 14 | Effect of void ratio (= 10^4 kPa, = 0.30, = 1 m, = 2.65, = 1.40).

The EOM of mixture (Equation (40)) and the time-integration formula (Equation (42)) correspond to Equation (11-1) and Equation (24), respectively, with a reduced order of dimensionless time derivatives. The rate-type SWCE (Equation (41)) is derived by taking the dimensionless time derivative of Equation (11-2). Additionally, Case [3] represents the basic combination discussed in the earlier section.

The results for Cases [1]–[4] are plotted in Figure 16, yielding the following observations:

10970207, 2025, 21, Downloaded from https://onlinelibrary.wiley.com/doi/10.1002/nme.70164 by Nagoya University, Wiley Online Library on [07/10/2026]. See the Terms and Conditions (https://onlinelibrary.wiley.com/terms-and-conditions) on Wiley Online Library for rules of use; OA articles are governed by the applicable Creative Commons License

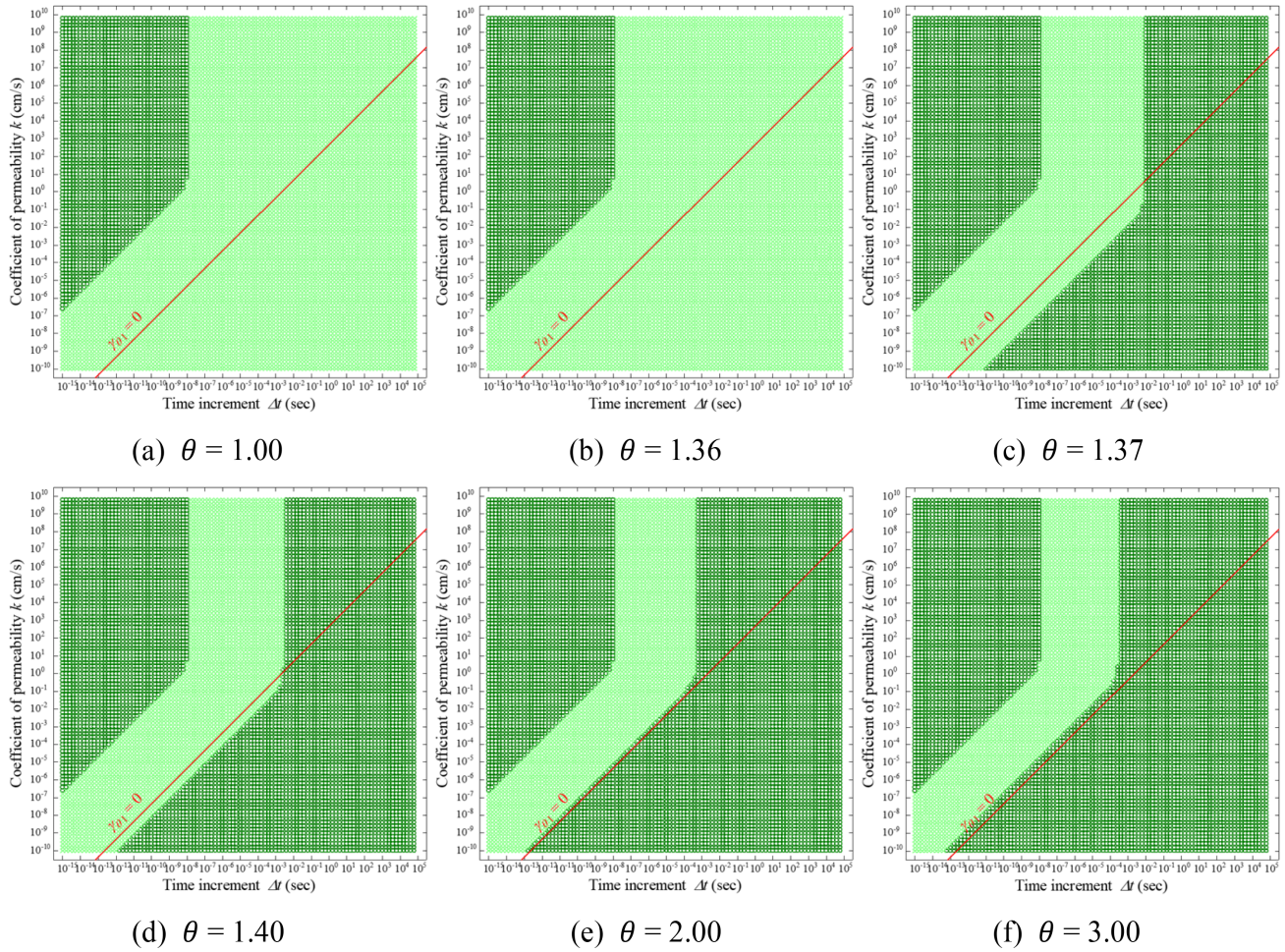


FIGURE 15 | Effect of ($= 10^4$ kPa, $= 0.30$, $= 1$ m, $= 2.65$, $= 1.0$).

TABLE 3 | Combinations of governing equations and linearity time integration formulae.

	Governing equations		Assumed linearity in time integration formulae	
Case	**EOM of mixture**	**SWCE**	**Linearity (displacement)**	**Linearity (pressure)**
[1]	—	—	Acceleration $\overset{\circ\circ}{U}_s$	Pressure rate $\mathring{P}$
[2]	—	—	Jerk $\overset{\circ\circ\circ}{U}_s$	Pressure rate $\mathring{P}$
[3]	Rate-type	—	Jerk $\overset{\circ\circ\circ}{U}_s$	Pressure rate $\mathring{P}$
[4]	Rate-type	Rate-type	Jerk $\overset{\circ\circ\circ}{U}_s$	Pressure rate $\mathring{P}$

- Comparing [3] in Figure 16a with [1] in Figure 16c: Simultaneously increasing the orders of the EOM and the time-integration formula does not significantly affect the global unstable region, although an unstable region appears in the low-permeability range with large time increments. It suggested that the instability appeared when adopting the "rate-type" EOM persists even when adopting a standard second-order EOM without jerk term.
- Comparing [4] in Figure 16c with [3] in Figure 16d: Adopting the rate-type SWCE along with the EOM does not result in significant changes in stability, despite the emergence of an unstable region in the low-permeability range with large time increments.
- Comparing [2] in Figure 16c with [1] in Figure 16a: A significant loss of stability occurs due to the excessive use of a higher-order time-integration formula applied to governing equations of ordinary order.

10970207, 2025, 21, Downloaded from https://onlinelibrary.wiley.com/doi/10.1002/nme.70164 by Nagoya University, Wiley Online Library on [07/10/2026]. See the Terms and Conditions (https://onlinelibrary.wiley.com/terms-and-conditions) on Wiley Online Library for rules of use; OA articles are governed by the applicable Creative Commons License

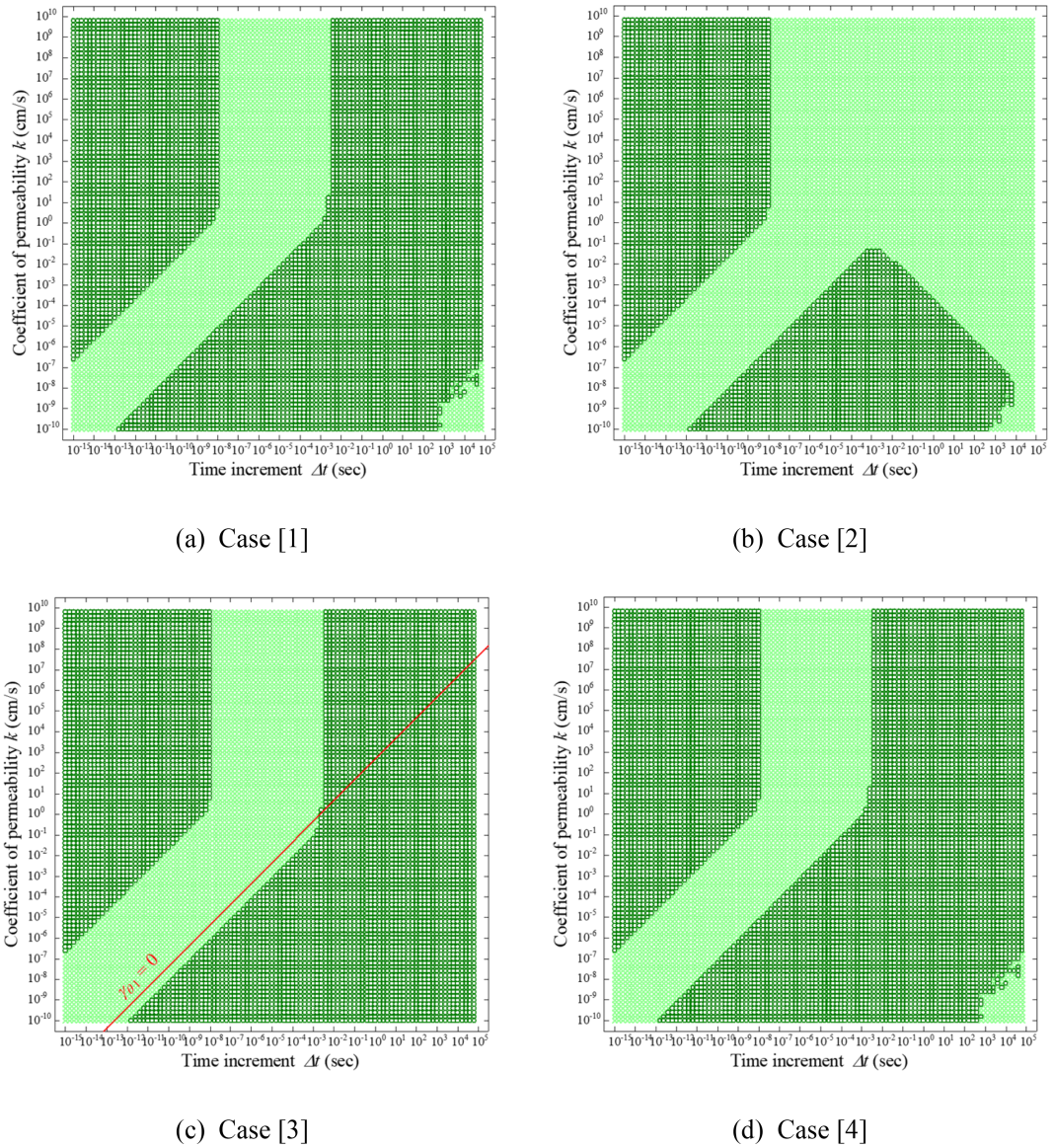


FIGURE 16 | Effect of combination of ordinary/rate-type governing equations with time integration formula assuming linearity of dimensionless acceleration/jerk term of solid phase ($Ev = 10^4$ kPa, = 0.30, = 1 m, = 2.65, = 1.0, = 1.40).

4.3 | Newmark's β Method

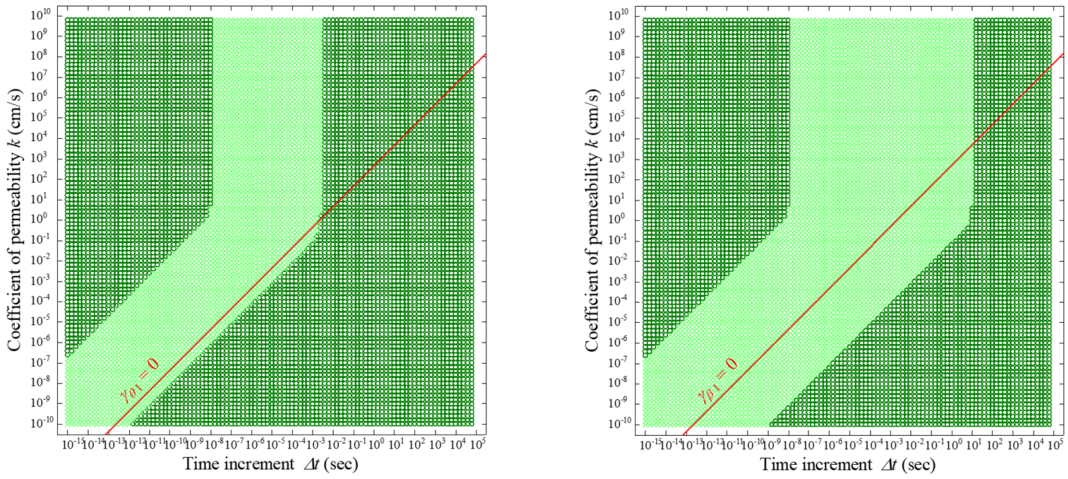
Here, we demonstrate that the same tendency of numerical stability can be observed when applying *Newmark-β* instead of *Wilson-θ*, as supplementary information.

4.3.1 | Formulation

Assuming the interpolation of the dimensionless jerk term between $T = T$ and $T = T + \Delta T$ as an extension of *Newmark-β* for the jerk term:

$$\left\{ \overset{\circ\circ\circ}{U}_s^{\mathrm{N}} \right\}\Big|_{T+\tau} = \left\{ \overset{\circ\circ\circ}{U}_s^{\mathrm{N}} \right\}\Big|_{T} + g(\tau)\left(\left\{ \overset{\circ\circ\circ}{U}_s^{\mathrm{N}} \right\}\Big|_{T+\Delta T} - \left\{ \overset{\circ\circ\circ}{U}_s^{\mathrm{N}} \right\}\Big|_{T} \right). \tag{43}$$

10970207, 2025, 21, Downloaded from https://onlinelibrary.wiley.com/doi/10.1002/nme.70164 by Nagoya University, Wiley Online Library on [07/10/2026]. See the Terms and Conditions (https://onlinelibrary.wiley.com/terms-and-conditions) on Wiley Online Library for rules of use; OA articles are governed by the applicable Creative Commons License



(a) *Wilson-θ* ($\theta = 1.40$) (b) *Newmark-β* ($\gamma = 0.50, \beta = 0.25$)

FIGURE 17 | Comparison of implicit time integration formulae (= 10^4 kPa, = 0.30, = 1 m, = 2.65, = 1.0).

Dimensionless time integration of Equation (32) sequentially leads to:

$$\left\{(\Delta T)^2 \overset{\circ\circ}{U}{}_s^{\mathrm{N}}\right\}\Big|_{T+\Delta T} = \left\{(\Delta T)^2 \overset{\circ\circ}{U}{}_s^{\mathrm{N}}\right\}\Big|_{T} + (1-\gamma)\left\{(\Delta T)^3 \overset{\circ\circ\circ}{U}{}_s^{\mathrm{N}}\right\}\Big|_{T} + \gamma\left\{(\Delta T)^3 \overset{\circ\circ\circ}{U}{}_s^{\mathrm{N}}\right\}\Big|_{T+\Delta T}, \tag{44-1}$$

$$\left\{(\Delta T)\mathring{U}_s^{\mathrm{N}}\right\}\Big|_{T+\Delta T} = \left\{(\Delta T)\mathring{U}_s^{\mathrm{N}}\right\}\Big|_{T} + \left\{(\Delta T)^2 \overset{\circ\circ}{U}{}_s^{\mathrm{N}}\right\}\Big|_{T} + \left(\frac{1}{2}-\beta\right)\left\{(\Delta T)^3 \overset{\circ\circ\circ}{U}{}_s^{\mathrm{N}}\right\}\Big|_{T} + \beta\left\{(\Delta T)^3 \overset{\circ\circ\circ}{U}{}_s^{\mathrm{N}}\right\}\Big|_{T+\Delta T}, \tag{44-2}$$

where γ and β are parameters from *Newmark-β* depending on $g(\tau)$. Setting $g(\tau) = 1/2$ corresponding to the averaged constant "jerk" method for the rate-type equation (corresponding to the averaged constant acceleration method for non-rate-type equations), results in $\gamma = 1/2$, $\beta = 1/4$, ensuring unconditional stability [18]. The trapezoidal rule for dimensionless pressure can be expressed as:

$$\left\{P^{\mathrm{E}}\right\}\Big|_{T+\Delta T} - \left\{P^{\mathrm{E}}\right\}\Big|_{T} = \frac{1}{2}\left(\left\{(\theta\Delta T)\mathring{P}^{\mathrm{E}}\right\}\Big|_{T} + \left\{(\theta\Delta T)\mathring{P}^{\mathrm{E}}\right\}\Big|_{T+\Delta T}\right). \tag{45}$$

Assuming Equations (21) and (23) are satisfied at dimensionless time $T = T + \Delta T$ with Equations (44-1), (44-2), and (45), the relation between the states at $T = T$ (at the n-th step) and $T = T + \Delta T$ (at $(n+1)$-th step) becomes:

$$\mathrm{F}\boldsymbol{u}_{n+1} = \mathrm{G}\boldsymbol{u}_n. \tag{46}$$

Therefore,

$$\boldsymbol{u}_{n+1} = \mathrm{E}\boldsymbol{u}_n, \mathrm{E} = \mathrm{F}^{-1}\mathrm{G}, \tag{47}$$

where the concrete forms of the matrices F and G are included in Appendix A: Specific Form of Matrices in Simultaneous Recursive Equations.

4.3.2 | Results

We investigated the spectral radius of the matrix E in Equation (47) using Newmark's β method setting $\gamma = 0.50$ and $\beta = 0.25$ as parameters to achieve unconditional convergence for a single-phase system [18]. The stable/unstable range is plotted in Figure 17b.

Compared with *Wilson-θ* in Figure 17a, *Newmark-β* exhibits a similar bending unstable band. However, the unstable band obtained by *Newmark-β* is thicker than that of *Wilson-θ*. Therefore, *Wilson-θ* demonstrates superior numerical stability compared to *Newmark-β*.

10970207, 2025, 21, Downloaded from https://onlinelibrary.wiley.com/doi/10.1002/nme.70164 by Nagoya University, Wiley Online Library on [07/10/2026]. See the Terms and Conditions (https://onlinelibrary.wiley.com/terms-and-conditions) on Wiley Online Library for rules of use; OA articles are governed by the applicable Creative Commons License

Additionally, the stability criterion for *Newmark-β* can be derived similarly to the $\gamma_{\theta 1}$ criterion for *Wilson-θ* as

$$\gamma_{\beta 1} = \beta - \frac{\gamma}{\Delta t}\frac{\rho^f k}{\gamma_w} > 0, \frac{k}{\Delta t} < \frac{\beta \gamma_w}{\gamma \rho^f} \ldots \text{Stable} \tag{48}$$

Assuming linearity of the jerk term, the stability threshold $\gamma_{\beta 1} = 0$, plotted in Figure 17b, is parallel to the boundary of the stable and unstable regions in the low-permeability range.

5 | Conclusion

This study investigated the stable range of ***u***-*p* using the spectral radius of the simultaneous recursive equation. The main findings are as follows:

- The "band-shaped" unstable region of ***u***-*p* (unstable band) on the permeability coefficient k-time increment Δt plane was identified.
- The band bent at the threshold between the overdamped and underdamped regions of the ***u***-*p* theoretical solution. The numerical stability of ***u***-*p* depended on $k/\Delta t$ in the low-permeability range (overdamped region) and on Δt in the high-permeability range (underdamped region).
- The rotation of the eigenvector of the diverging eigenmode near the bend led to significant differences in the nature of numerical divergence between the low- and high-permeability ranges. In the low-permeability range, only diverging oscillations of the checkerboard pressure distribution were observed, whereas numerical divergence in the high-permeability range was accompanied by the divergence of solid-phase deformation.
- The $\gamma_{\theta 1}$ criterion proposed by Noda et al. [5], which evaluates the feasibility of ***u***-*p*-based numerical simulations based on $k/\Delta t$, was generally valid only in the low-permeability range. Although the illogical phenomenon underlying the $\gamma_{\theta 1}$ criterion — namely, the violation of SWCE — was not observed in the diverging eigenmode, a tendency for illogical distributions was evident in the higher-order derivatives of volumetric strain.
- Supplementary findings regarding the appearance of the unstable region of ***u***-*p* were as follows:
  - An increase in one-dimensional stiffness E_c or a decrease in thickness H equivalent to simultaneous increases in the permeability coefficient k and time increment Δt in terms of numerical stability did not affect the threshold of ***u***-*p* in the low-permeability range. Changes in specific gravity G_s and void ratio e had no significant impact on the unstable region. The condition for unconditional stability of *Wilson-θ* $\theta > 1.37$ remained valid as a prerequisite for stability in soil-water coupled analysis.
  - Simultaneous increases in the orders of the EOM and the time-integration formula, as well as the adoption of the rate-type SWCE alongside the EOM, did not significantly affect the unstable region overall. However, the excessive application of higher-order time-integration formulas to governing equations resulted in critical instability.
  - *Newmark-β* exhibited the same general appearance of the unstable range of ***u***-*p* as *Wilson-θ*.

In future work, we will demonstrate that the *Full* formulation exhibits unconditional stability in numerical simulations, highlighting its versatile applicability. Furthermore, the discrepancies between the ***u***-*p* and *Full* formulations as conditions approach the unstable band will be examined in greater detail.

Author Contributions

Tomohiro Toyoda: conceptualization, methodology, software, investigation, writing – original draft. Toshihiro Noda: supervision, writing – review and editing.

Acknowledgments

This work was supported by JSPS KAKENHI (Grant Number 22K14324).

Data Availability Statement

The data that support the findings of this study are available from the corresponding author upon reasonable request.

10970207, 2025, 21, Downloaded from https://onlinelibrary.wiley.com/doi/10.1002/nme.70164 by Nagoya University, Wiley Online Library on [07/10/2026]. See the Terms and Conditions (https://onlinelibrary.wiley.com/terms-and-conditions) on Wiley Online Library for rules of use; OA articles are governed by the applicable Creative Commons License

References

1. M. A. Biot, "General Theory of Three-Dimensional Consolidation," *Journal of Applied Physics* 12 (1941): 155–164, https://doi.org/10.1063/1.1712886.

2. M. A. Biot, "Mechanics of Deformation and Acoustic Propagation in Porous Media," *Journal of Applied Physics* 33 (1962): 1482–1498, https://doi.org/10.1063/1.1728759.

3. P. Fillunger, *Erdbaumechanik?* (Selbstvrlag des Verfassers, 1936) (in German).

4. O. C. Zienkiewicz, C. T. Chang, and P. Bettess, "Drained, Undrained, Consolidating and Dynamic Behaviour Assumptions in Soils," *Géotechnique* 30 (1980): 385–395, https://doi.org/10.1680/geot.1980.30.4.385.

5. T. Noda, A. Asaoka, and M. Nakano, "Soil-Water Coupled Finite Deformation Analysis Based on a Rate-Type Equation of Motion Incorporating the SYS Cam-Clay Model," *Soils and Foundations* 48 (2008): 771–790, https://doi.org/10.3208/sandf.48.771.

6. T. Toyoda and T. Noda, "Unconditional Convergence of Theoretical Solutions to ***u***-*p* Formulation," *Soils and Foundations* 64 (2024): 101421, https://doi.org/10.1016/j.sandf.2023.101421.

7. T. Noda and T. Toyoda, "Development and Verification of a Soil-Water Coupled Finite Deformation Analysis Based on ***u***-*p* Formulation With Fluid Convective Nonlinearity," *Soils and Foundations* 59 (2019): 888–904, https://doi.org/10.1016/j.sandf.2019.03.008.

8. F. Oka, A. Yashima, T. Shibata, M. Kato, and R. Uzuoka, "FEM-FDM Coupled Liquefaction Analysis of a Porous Soil Using an Elasto-Plastic Model," *Applied Scientific Research* 52 (1994): 209–245, https://doi.org/10.1007/BF00853951.

9. O. C. Zienkiewicz and P. Bettess, "Soils and Other Saturated Media Under Transient, Dynamic Conditions; General Foundation and the Validity of Various Simplifying Assumptions," in *Soil Mechanics – Transient and Cyclic Loads: Constitutive Relations and Numerical Treatment*, ed. G. N. Pande and O. C. Zienkiewicz (John Wiley & Sons, 1982).

10. O. C. Zienkiewicz, C. T. Chang, M. Pastor, D. K. Paul, and T. Shiomi, "Static and Dynamic Behaviour of Soils: A Rational Approach to Quantitative Solutions. i. Fully Saturated Problems," *Proceedings of the Royal Society of London. Series A: Mathematical and Physical Sciences* 429 (1990): 285–309, https://doi.org/10.1098/rspa.1990.0061.

11. O. C. Zienkiewicz, C. T. Chang, M. Pastor, B. A. Schrefler, and T. Shiomi, *Computational Geomechanics With Special Reference to Earthquake Engineering* (John Wiley & Sons, 1999).

12. J. H. Prevost, "Wave Propagation in Fluid-Saturated Porous Media: An Efficient Finite Element Procedure," *International Journal of Soil Dynamics and Earthquake Engineering* 4 (1985): 183–202, https://doi.org/10.1016/0261-7277(85)90038-5.

13. B. R. Simon, J. S. S. Wu, O. C. Zienkiewicz, and D. K. Paul, "Evaluation of u – W and u – π Finite Element Methods for the Dynamic Response of Saturated Porous Media Using One-Dimensional Models," *International Journal for Numerical and Analytical Methods in Geomechanics* 10 (1986): 461–482, https://doi.org/10.1002/nag.1610100502.

14. E. L. Wilson, I. Farhoomand, and K. J. Bathe, "Nonlinear Dynamic Analysis of Complex Structures," *Earthquake Engineering and Structural Dynamics* 1 (1972): 241–252, https://doi.org/10.1002/eqe.4290010305.

15. M. Kato, "Study on Multidimensional Liquefaction Analysis Method and Its Application," 1995 (PhD thesis, Gifu University, 1995) (in Japanese).

16. E. J. Routh, *A Treatise on the Stability of a Given State of Motion: Particularly Steady Motion* (MacMillan, 1877).

17. A. Hurwitz, "Ueber die Bedingungen, unter welchen eine Gleichung nur Wurzeln mit negativen reellen Theilen besitzt," *Mathematische Annalen* 46 (1895): 273–284. (in German), https://doi.org/10.1007/BF01446812.

18. N. M. Newmark, "A Method of Computation for Structural Dynamics," *Journal of the Engineering Mechanics Division* 85 (1959): 67–94, https://doi.org/10.1061/JMCEA3.0000098.

19. N. Nishimura, "Chapter 3. Geotechnical Engineering Handbook," in *Soil Mechanics* (Japanese Geotechnical Society, 1999) (in Japanese).

20. C. Yatomi, A. Yashima, A. Ilzuka, and I. Sano, "General Theory of Shear Bands Formation by a Non-Coaxial Cam-Clay Model," *Soils and Foundations* 29 (1989): 41–53, https://doi.org/10.3208/sandf1972.29.3_41.

21. V. R. Osinov, "The *u-p* Approximation Versus the Exact Dynamic Equations for Anisotropic Fluid-Saturated Solids. I. Hyperbolicity," *International Journal for Numerical and Analytical Methods in Geomechanics* 48 (2023): 396–418, https://doi.org/10.1002/nag.3645.

22. A. Asaoka, M. Nakano, and T. Noda, "Soil-Water Coupled Behaviour of Saturated Clay Near/at Critical State," *Soils and Foundations* 34 (1994): 91–105, https://doi.org/10.3208/sandf1972.34.91.

23. J. T. Christian, "Undrained Stress Distribution by Numerical Methods," *Journal of the Soil Mechanics and Foundations Division* 94 (1968): 1333–1345, https://doi.org/10.1061/JSFEAQ.0001199.

24. K. Akai and T. Tamura, "Numerical Analysis of Multi-Dimensional Consolidation Accompanied With Elasto-Plastic Constitutive Equation," *Proceedings. Japan Society of Civil Engineers* 1978 (1978): 95–104, https://doi.org/10.2208/jscej1969.1978.95.

10970207, 2025, 21, Downloaded from https://onlinelibrary.wiley.com/doi/10.1002/nme.70164 by Nagoya University, Wiley Online Library on [07/10/2026]. See the Terms and Conditions (https://onlinelibrary.wiley.com/terms-and-conditions) on Wiley Online Library for rules of use; OA articles are governed by the applicable Creative Commons License

25. K. J. Bathe and E. L. Wilson, "Stability and Accuracy Analysis of Direct Integration Methods," *Earthquake Engineering and Structural Dynamics* 1 (1972): 283–291, https://doi.org/10.1002/eqe.4290010308.

Appendix A

Detailed Derivation of Discretized Governing Equation With Concrete Forms of Matrices and Vectors

Derivation of Discretized Dimensionless Rate-Type EOM

Linear interpolations of the dimensionless displacement $U_s(Z,T)$ and the arbitrary dimensionless function $\delta V(Z,T)$ in an element are written as:

$$U_s(Z,T) = \sum_{k=1}^{2} N^{(k)}(Z) U_s^{(k)}(T) = [N]\{U_{se}\}, \tag{A1-1}$$

$$\delta V(Z,T) = \sum_{k=1}^{2} N^{(k)}(Z) U_s^{(k)}(T) = [N]\{\delta V_e\}, \tag{A1-2}$$

where $N^{(k)}$ represents the shape function of an element written as follows:

$$N^{(1)}(Z) = \frac{Z^{(2)} - Z}{\Delta Z}, N^{(2)}(Z) = \frac{Z - Z^{(1)}}{\Delta Z}, \tag{A2}$$

$\Delta Z = Z^{(2)} - Z^{(1)}$ is the thickness of the element with the superscript (k) $(k = 1, 2)$ denoting the local node numbers at the element, $[N]$, $\{U_{se}\}$, and $\{\delta V_e\}$ are the shape function matrix and the element-wise coefficient vectors expressed as:

$$[N] = \begin{bmatrix} N^{(1)} & N^{(2)} \end{bmatrix}, \{U_{se}\} = \begin{Bmatrix} U_s^{(1)} \\ U_s^{(2)} \end{Bmatrix}, \{\delta V_e\} = \begin{Bmatrix} \delta V^{(1)} \\ \delta V^{(2)} \end{Bmatrix}. \tag{A3}$$

The correspondence of the shape functions of U_s and δV in Equations (A1-1) and (A1-2) follows the Galerkin method. The spatial gradients of U_s and δV are written with the $[B]$ matrix as:

$$\frac{dU_s}{dZ}(Z,T) = \sum_{k=1}^{2} \frac{dN^{(k)}(Z)}{dZ} U_s^{(k)}(T) = [B]\{U_{se}\}, \tag{A4-1}$$

$$\frac{d\delta V}{dZ}(Z,T) = \sum_{k=1}^{2} \frac{dN^{(k)}(Z)}{dZ} U_s^{(k)}(T) = [B]\{\delta V_e\}, \tag{A4-2}$$

where

$$[B] = \begin{bmatrix} \frac{dN^{(1)}}{dZ} & \frac{dN^{(2)}}{dZ} \end{bmatrix}. \tag{A5}$$

Thus, the weak form of the dimensionless rate-type EOM Equation (20) is written as:

$$\{\delta V^*\}^{\mathrm{T}} \left(\frac{\mathrm{e}(G_s + \mathrm{e})}{1 + G_s \mathrm{e}} [\mathrm{M}^*] \left\{ \overset{\circ\circ\circ}{U}{}_s^* \right\} + 4h^2 [\mathrm{K}^*] \left\{ \mathring{U}_s^* \right\} - 4h^2 [\mathrm{L}^*]^{\mathrm{T}} \left\{ \mathring{P}^* \right\} \right) = 0, \tag{A6}$$

where $\{U_s^*\}$, $\{\delta V^*\}$, and $\{P^*\}$ denote the extended coefficient vectors expressed as:

$$\{U_s^*\} = \begin{Bmatrix} U_s^0 \\ U_s^1 \\ U_s^2 \\ \vdots \\ U_s^{m-1} \\ U_s^m \end{Bmatrix}, \{\delta V^*\} = \begin{Bmatrix} \delta V^0 \\ \delta V^1 \\ \delta V^2 \\ \vdots \\ \delta V^{m-1} \\ \delta V^m \end{Bmatrix}, \{P^*\} = \begin{Bmatrix} P^1 \\ P^2 \\ P^3 \\ \vdots \\ P^m \end{Bmatrix}, \tag{A7}$$

10970207, 2025, 21, Downloaded from https://onlinelibrary.wiley.com/doi/10.1002/nme.70164 by Nagoya University, Wiley Online Library on [07/10/2026]. See the Terms and Conditions (https://onlinelibrary.wiley.com/terms-and-conditions) on Wiley Online Library for rules of use; OA articles are governed by the applicable Creative Commons License

where $\left[\mathrm{M}^*\right]$, $\left[\mathrm{K}^*\right]$, and $\left[\mathrm{L}^*\right]$ are the extended coefficient matrices denoted as:

$$\left[\mathrm{M}^*\right]=\sum_e\left[\mathrm{M}_e\right]=\frac{\Delta Z}{6}\begin{bmatrix}2&1&&&&\\1&4&1&&&\\&1&4&1&&\\&&1&\ddots&1&\\&&&1&4&1\\&&&&1&2\end{bmatrix}, \tag{A8-1}$$

$$\left[\mathrm{K}^*\right]=\sum_e\left[\mathrm{K}_e\right]=\frac{1}{\Delta Z}\begin{bmatrix}1&-1&&&&\\-1&2&-1&&&\\&-1&2&-1&&\\&&-1&\ddots&-1&\\&&&-1&2&-1\\&&&&-1&1\end{bmatrix}, \tag{A8-2}$$

$$\left[\mathrm{L}^*\right]=\sum_e\left[\mathrm{L}_e\right]=\begin{bmatrix}-1&1&&&&\\&-1&1&&&\\&&\ddots&&&\\&&&-1&1&\\&&&&-1&1\end{bmatrix}, \tag{A8-3}$$

where $\left[\mathrm{M}_e\right]$, $\left[\mathrm{K}_e\right]$, and $\left[\mathrm{L}_e\right]$ represent the local mass, stiffness, and displacement-volume change converter matrices of each element.

$$\left[\mathrm{M}_e\right]=\int_{X^{(1)}}^{X^{(2)}}[N]^{\mathrm{T}}[N]dX=\frac{\Delta Z}{6}\begin{bmatrix}2&1\\1&2\end{bmatrix}, \tag{A9-1}$$

$$\left[\mathrm{K}_e\right]=\int_{X^{(1)}}^{X^{(2)}}[B]^{\mathrm{T}}[B]dX=\frac{1}{\Delta Z}\begin{bmatrix}1&-1\\-1&1\end{bmatrix}, \tag{A9-2}$$

$$\left[\mathrm{L}_e\right]=\int_{X^{(1)}}^{X^{(2)}}[B]dX=\begin{bmatrix}-1&1\end{bmatrix}. \tag{A9-3}$$

Considering the Dirichlet boundary condition in Equation (15-1), that is, $U_s(0,T)=U_s^0=0$, and the requirement for the dimensionless arbitrary function $\delta V(0,T)=\delta V^0=0$, Equation (A6) becomes

$$\left\{\delta V^{\mathrm{N}}\right\}^{\mathrm{T}}\left(\frac{\mathrm{e}\left(G_s+\mathrm{e}\right)}{1+G_s\mathrm{e}}[\mathrm{M}]\left\{\begin{matrix}\overset{\circ\circ\circ}{U}{}_s^{\mathrm{N}}\end{matrix}\right\}+4h^2[\mathrm{K}]\left\{\mathring{U}_s^{\mathrm{N}}\right\}-4h^2[\mathrm{L}]^{\mathrm{T}}\left\{\mathring{P}^{\mathrm{E}}\right\}\right)=0, \tag{A10}$$

where $\left\{U_s^{\mathrm{N}}\right\}$, $\left\{\delta V^{\mathrm{N}}\right\}$, and $\left\{P^{\mathbf{E}}\right\}$ denote the global coefficient vectors:

$$\left\{U_s^{\mathrm{N}}\right\}=\begin{Bmatrix}U_s^1\\U_s^2\\\vdots\\U_s^{m-1}\\U_s^m\end{Bmatrix},\left\{\delta V^{\mathrm{N}}\right\}=\begin{Bmatrix}\delta V^1\\\delta V^2\\\vdots\\\delta V^{m-1}\\\delta V^m\end{Bmatrix},\left\{P^{\mathrm{E}}\right\}=\begin{Bmatrix}P^1\\P^2\\\vdots\\P^{m-1}\\P^m\end{Bmatrix}, \tag{A11}$$

where the global mass, stiffness, and displacement-volume change converter matrices are denoted as [M], [K], and [L], respectively:

$$[\mathrm{M}]=\frac{\Delta Z}{6}\begin{bmatrix}4&1&&&\\1&4&1&&\\&1&\ddots&1&\\&&1&4&1\\&&&1&2\end{bmatrix}, \tag{A12-1}$$

10970207, 2025, 21, Downloaded from https://onlinelibrary.wiley.com/doi/10.1002/nme.70164 by Nagoya University, Wiley Online Library on [07/10/2026]. See the Terms and Conditions (https://onlinelibrary.wiley.com/terms-and-conditions) on Wiley Online Library for rules of use; OA articles are governed by the applicable Creative Commons License

$$[\mathrm{K}] = \sum_e [\mathrm{K}_e] = \frac{1}{\Delta Z}\begin{bmatrix} 2 & -1 & & & & \\ -1 & 2 & -1 & & & \\ & -1 & \ddots & -1 & & \\ & & -1 & 2 & -1 & \\ & & & -1 & 1 & \end{bmatrix}, \tag{A12-2}$$

$$[\mathrm{L}] = \sum_e [\mathrm{L}_e] = \begin{bmatrix} 1 & & & & & \\ -1 & 1 & & & & \\ & \ddots & & & & \\ & & -1 & 1 & & \\ & & & -1 & 1 & \end{bmatrix}, \tag{A12-3}$$

where the components of these matrices were treated considering the boundary conditions. Considering the arbitrariness of $\{\delta V^{\mathrm{N}}\}$, Equation (21) was obtained.

Formulation of Dimensionless Physical Model of Seepage

We obtained the discretization of the diffusion term, that is, the third term of Equation (11-2), based on the method proposed by Christian and Tamura. Focusing on the i-th element and the adjacent $(i+1)$-th element shown in Figure A1, the dimensionless averaged flow rates from the center of the i-th element toward the boundary $W^{(i)}$ and from the boundary toward the center of the $(i+1)$-th element $W^{(i+1)}$ can be expressed as:

$$W^{(i)} = -\frac{P^{(c)} - P^i}{\Delta Z/2} - \frac{\mathrm{e}(1+\mathrm{e})}{1+G_s\mathrm{e}}\frac{1}{4h^2}\overset{\circ\circ(c)}{U_s}, \tag{A13-1}$$

$$W^{(i+1)} = -\frac{P^{i+1} - P^{(c)}}{\Delta Z/2} - \frac{\mathrm{e}(1+\mathrm{e})}{1+G_s\mathrm{e}}\frac{1}{4h^2}\overset{\circ\circ(c)}{U_s}, \tag{A13-2}$$

where P^i denotes the dimensionless pressure at the i-th element, $P^{(c)}$ represents the dimensionless pressure on the boundary, and $\overset{\circ\circ(c)}{U_s}$ is the dimensionless solid acceleration at the boundary. From the continuity equation:

$$W^{(i+1)} = W^{(i)}. \tag{A14}$$

Substituting Equations (A13-1) and (A13-2) into Equation (A14), we obtained the dimensionless boundary pressure $P^{(c)}$ as:

$$P^{(c)} = \frac{P^i + P^{i+1}}{2}. \tag{A15}$$

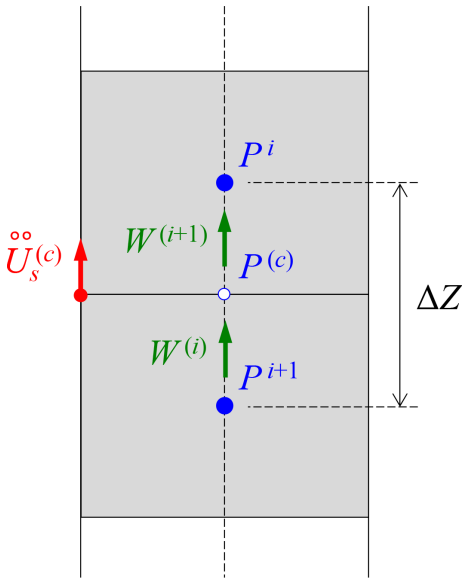


FIGURE A1 | Christian and Tamura's method.

10970207, 2025, 21, Downloaded from https://onlinelibrary.wiley.com/doi/10.1002/nme.70164 by Nagoya University, Wiley Online Library on [07/10/2026]. See the Terms and Conditions (https://onlinelibrary.wiley.com/terms-and-conditions) on Wiley Online Library for rules of use; OA articles are governed by the applicable Creative Commons License

For the hydraulic boundary pressures at each end of the domain:

$$\frac{\partial P^{(c)}}{\partial Z} = 0 \text{ at } Z = Z^1 = 0, \tag{A16-1}$$

$$P^{(c)} = 0 \text{ at } Z = Z^{m+1} = 1. \tag{A16-2}$$

Thus, the spatial integration of the diffusion term at the i-th element ($Z^{(1)} \le Z \le Z^{(2)}$) can be calculated as:

$$\int_{Z^{(1)}}^{Z^{(2)}} \frac{\partial^2 P}{\partial Z^2} dX = \left.\frac{\partial P}{\partial Z}\right|_{Z^{(2)}} - \left.\frac{\partial P}{\partial Z}\right|_{Z^{(1)}} = \frac{P|_{Z^{(2)}} - P^i}{\Delta Z/2} - \frac{P^i - P|_{Z^{(1)}}}{\Delta Z/2} = \begin{cases} \frac{-P^1+P^2}{\Delta Z} & (\text{elem } 1) \\ \frac{P^{i-1}-2P^i+P^{i+1}}{\Delta Z} & (\text{elem } 2 \sim m-1) \\ \frac{P^{m-1}-3P^m}{\Delta Z} & (\text{elem } m) \end{cases}. \tag{A17}$$

Derivation of Discretized Dimensionless SWCE

Substituting the linear interpolation of U_s and the discretization of P from Equations (A1-1) and (A17), Equation (22) can be written as:

$$-\frac{\mathrm{e}(1+\mathrm{e})}{1+G_s\mathrm{e}}[\mathrm{L}]\left\{\begin{matrix}\overset{\circ\circ}{U}{}_s^{\mathrm{N}}\end{matrix}\right\} + 4h^2[\mathrm{L}]\left\{\overset{\circ}{U}{}_s^{\mathrm{N}}\right\} + 4h^2[\mathrm{H}]\left\{P^{\mathrm{E}}\right\} = 0, \tag{A18}$$

where H is the discretized Laplacian operator matrix expressed as:

$$[\mathrm{H}] = \frac{1}{\Delta Z}\begin{bmatrix} 1 & -1 & & & \\ -1 & 2 & -1 & & \\ & -1 & 2 & -1 & \\ & & & \ddots & \\ & & & -1 & 3 \end{bmatrix}. \tag{A19}$$

Considering the Dirichlet boundary condition in Equation (13-1), we obtained Equation (22).

Calculation of Elemental Dimensionless Volumetric Strain and Its Derivatives

Defining compression as positive, the elemental volumetric strain of the i-th element, ε^i, can be calculated as the axial strain in the one-dimensional case as:

$$\varepsilon^i = \frac{U_s^{i+1} - U_s^i}{\Delta Z}, \tag{A20-1}$$

where its derivative (strain rate and higher-order terms) can be calculated as:

$$\overset{\circ}{\varepsilon}{}^i = \frac{\overset{\circ}{U}{}_s^{i+1} - \overset{\circ}{U}{}_s^i}{\Delta Z}, \overset{\circ\circ}{\varepsilon}{}^i = \frac{\overset{\circ\circ}{U}{}_s^{i+1} - \overset{\circ\circ}{U}{}_s^i}{\Delta Z}, \overset{\circ\circ\circ}{\varepsilon}{}^i = \frac{\overset{\circ\circ\circ}{U}{}_s^{i+1} - \overset{\circ\circ\circ}{U}{}_s^i}{\Delta Z} \tag{A20-2}$$

Specific Form of Matrices in Simultaneous Recursive Equations

Wilson-θ

$$\mathrm{A} = \begin{bmatrix} \frac{1}{(\theta\Delta T)^2}\frac{\mathrm{e}(G_s+\mathrm{e})}{1+G_s\mathrm{e}}[\mathrm{M}] & [0] & 4h^2[\mathrm{K}] & -4h^2[\mathrm{L}]^{\mathrm{T}} & [0] \\ [0] & \frac{1}{\theta\Delta T}\frac{\mathrm{e}(1+\mathrm{e})}{1+G_s\mathrm{e}}[\mathrm{L}] & -4h^2[\mathrm{L}] & [0] & -4h^2(\theta\Delta T)[\mathrm{H}] \\ -\frac{1}{2}[1] & [1] & [0] & [0] & [0] \\ -\frac{1}{6}[1] & [0] & [1] & [0] & [0] \\ [0] & [0] & [0] & -\frac{1}{2}[1] & [1] \end{bmatrix}, \tag{A21-1}$$

$$\mathrm{B} = \begin{bmatrix} [0] & [0] & [0] & [0] & [0] \\ [0] & [0] & [0] & [0] & [0] \\ \frac{1}{2}[1] & [1] & [0] & [0] & [0] \\ \frac{1}{3}[1] & [1] & [1] & [0] & [0] \\ [0] & [0] & [0] & \frac{1}{2}[1] & [1] \end{bmatrix}, \tag{A21-2}$$

10970207, 2025, 21, Downloaded from https://onlinelibrary.wiley.com/doi/10.1002/nme.70164 by Nagoya University, Wiley Online Library on [07/10/2026]. See the Terms and Conditions (https://onlinelibrary.wiley.com/terms-and-conditions) on Wiley Online Library for rules of use; OA articles are governed by the applicable Creative Commons License

$$\mathrm{C}=\begin{bmatrix} \left(1-\frac{1}{\theta}\right)[1] & [0] & [0] & [0] & [0] \\ \left(\frac{1}{\theta}-\frac{1}{2\theta^2}\right)[1] & [1] & [0] & [0] & [0] \\ \left(\frac{1}{2\theta^2}-\frac{1}{6\theta^3}\right)[1] & \frac{1}{\theta}[1] & [1] & [0] & [0] \\ [0] & [0] & [0] & \left(1-\frac{1}{\theta}\right)[1] & [0] \\ [0] & [0] & [0] & \left(\frac{1}{\theta}-\frac{1}{2\theta^2}\right)[1] & [1] \end{bmatrix}, \tag{A21-3}$$

$$\mathrm{D}=\begin{bmatrix} \frac{1}{\theta}[1] & [0] & [0] & [0] & [0] \\ \frac{1}{2\theta^2}[1] & [0] & [0] & [0] & [0] \\ \frac{1}{6\theta^3}[1] & [0] & [0] & [0] & [0] \\ [0] & [0] & [0] & \frac{1}{\theta}[1] & [0] \\ [0] & [0] & [0] & \frac{1}{2\theta^2}[1] & [0] \end{bmatrix}, \tag{A21-4}$$

where [0] is the zero matrix, and [1] is the identity matrix.

Newmark-β

$$\mathrm{F}=\begin{bmatrix} \frac{1}{(\Delta T)^2}\frac{\mathrm{e}(G_s+\mathrm{e})}{1+G_s\mathrm{e}}[\mathrm{M}] & [0] & 4h^2[\mathrm{K}] & -4h^2[\mathrm{L}]^{\mathrm{T}} & [0] \\ [0] & \frac{1}{\Delta T}\frac{\mathrm{e}(1+\mathrm{e})}{1+G_s\mathrm{e}}[\mathrm{L}] & -4h^2[\mathrm{L}] & [0] & 4h^2(\Delta T)[\mathrm{H}] \\ -\gamma[1] & [1] & [0] & [0] & [0] \\ -\beta[1] & [0] & [1] & [0] & [0] \\ [0] & [0] & [0] & -\frac{1}{2}[1] & [1] \end{bmatrix}, \tag{A22-1}$$

$$\mathrm{G}=\begin{bmatrix} [0] & [0] & [0] & [0] & [0] \\ [0] & [0] & [0] & [0] & [0] \\ (1-\gamma)[1] & [1] & [0] & [0] & [0] \\ \left(\frac{1}{2}-\beta\right)[1] & [1] & [1] & [0] & [0] \\ [0] & [0] & [0] & \frac{1}{2}[1] & [1] \end{bmatrix}. \tag{A22-2}$$

Single-Phase Stability Analysis

The single-phase analysis has been conducted preliminarily to ensure the validity of the proposed stability analysis.

Formulation of Single-Phase Analysis

The one-dimensional governing equation of single-phase analysis, that is, the wave equation considering damping, is expressed as:

$$\ddot{u}_s + 2\xi c\ddot{u}_s - c^2\frac{\partial^2 \dot{u}_s}{\partial z^2} = 0, \quad 0 < z < H, \quad t > 0, \tag{A23-1}$$

$$c = \sqrt{\frac{E_c}{\rho}}, \xi = \frac{\zeta}{2\sqrt{\rho E_c}}, \tag{A23-2}$$

where u_s denotes the displacement of the single-phase material, ρ, ζ, E_c denote density, attenuation coefficient, and stiffness of the single-phase material. c and ξ are the wave celerity and damping ratio. Boundary and initial conditions are set referring to Equations (7-1–7-2) as:

$$u_s(z=0,t) = 0, \quad t > 0, \tag{A24-1}$$

$$\frac{\partial u_s}{\partial z}(z=H,t) = -\frac{q}{E_c}, \quad t > 0. \tag{A24-2}$$

$$u_s(z,t=0) = 0, \quad 0 < z < H. \tag{A25}$$

10970207, 2025, 21, Downloaded from https://onlinelibrary.wiley.com/doi/10.1002/nme.70164 by Nagoya University, Wiley Online Library on [07/10/2026]. See the Terms and Conditions (https://onlinelibrary.wiley.com/terms-and-conditions) on Wiley Online Library for rules of use; OA articles are governed by the applicable Creative Commons License

By defining the dimensionless variables:

$$U_s = \frac{u_s}{S}, T = \frac{t}{t_p}, \quad Z = \frac{z}{H}, \quad S = \frac{qH}{E_c}, \tag{A26}$$

The dimensionless form of Equations (A23-1), (A24-1), (A24-2), and (A25) can be obtained as follows:

$$\overset{\circ\circ\circ}{U}_s + 2\Xi C \overset{\circ\circ}{U}_s - C^2 \frac{\partial^2 \overset{\circ}{U}_s}{\partial X^2} = 0, \quad 0 < Z < 1, \quad T > 0, \tag{A27-1}$$

$$C = \frac{ct_p}{H}, \Xi = \xi H, \tag{A27-2}$$

$$U_s(Z = 0, T) = 0, \quad T > 0, \tag{A28-1}$$

$$\frac{\partial U_s}{\partial Z}(Z = 1, T) = 1, \quad T > 0. \tag{A28-2}$$

$$U_s(Z, T = 0) = 0, \quad 0 < Z < 1. \tag{A29}$$

where U_s, T, and Z represent the dimensionless displacement, time, and position, respectively, $(\,)^\circ = \partial/\partial T$ is the dimensionless time derivative; S is the displacement due to the application of the static load q; t_p is a representative time; C and Ξ are the dimensionless wave celerity and damping ratio, respectively. Taking the weak form of Equation (A27-1) and applying spatial discretization similarly to Section 2.3.1, the discretized equation becomes:

$$[\mathrm{M}]\left\{\overset{\circ\circ\circ\mathrm{N}}{U_s}\right\} + 2\Xi C_p[\mathrm{M}]\left\{\overset{\circ\circ\mathrm{N}}{U_s}\right\} + C_p^2[\mathrm{K}]\left\{\overset{\circ\mathrm{N}}{U_s}\right\} = \{0\}. \tag{A30}$$

Using Wilson's θ method, the simultaneous recursive equation is derived in the same way as in Section 2.3.2, using Equations (26-1), (26-2), and (27) as:

$$\boldsymbol{u}_{n+1} = \mathrm{E}\boldsymbol{u}_n, \mathrm{E} = \mathrm{C} + \mathrm{D}\mathrm{A}^{-1}\mathrm{B}, \tag{A31}$$

where

$$\boldsymbol{u}_n = \begin{bmatrix} \left\{(\theta\Delta T)^3 \overset{\circ\circ\circ\mathrm{N}}{U_s}\right\} \\ \left\{(\theta\Delta T)^2 \overset{\circ\circ\mathrm{N}}{U_s}\right\} \\ \left\{(\theta\Delta T) \overset{\circ\mathrm{N}}{U_s}\right\} \end{bmatrix}\Bigg|_T, \boldsymbol{u}_{n+1} = \begin{bmatrix} \left\{(\theta\Delta T)^3 \overset{\circ\circ\circ\mathrm{N}}{U_s}\right\} \\ \left\{(\theta\Delta T)^2 \overset{\circ\circ\mathrm{N}}{U_s}\right\} \\ \left\{(\theta\Delta T) \overset{\circ\mathrm{N}}{U_s}\right\} \end{bmatrix}\Bigg|_{T+\Delta T}, \boldsymbol{u}_{n+\theta} = \begin{bmatrix} \left\{(\theta\Delta T)^3 \overset{\circ\circ\circ\mathrm{N}}{U_s}\right\} \\ \left\{(\theta\Delta T)^2 \overset{\circ\circ\mathrm{N}}{U_s}\right\} \\ \left\{(\theta\Delta T) \overset{\circ\mathrm{N}}{U_s}\right\} \end{bmatrix}\Bigg|_{T+\theta\Delta T}, \tag{A32}$$

$$\mathrm{A} = \begin{bmatrix} \frac{1}{(\theta\Delta T)^2}[\mathrm{M}] & \frac{2\Xi C}{\theta\Delta T}[\mathrm{M}] & C^2[\mathrm{K}] \\ -\frac{1}{2}[1] & [0] & [1] \\ -\frac{1}{6}[1] & [1] & [0] \end{bmatrix}, \tag{A33-1}$$

$$\mathrm{B} = \begin{bmatrix} [0] & [0] & [0] \\ \frac{1}{2}[1] & [1] & [0] \\ \frac{1}{3}[1] & [1] & [1] \end{bmatrix}, \tag{A33-2}$$

$$\mathrm{C} = \begin{bmatrix} \left(1 - \frac{1}{\theta}\right)[1] & [0] & [0] \\ \left(\frac{1}{\theta} - \frac{1}{2\theta^2}\right)[1] & [1] & [0] \\ \left(\frac{1}{2\theta^2} - \frac{1}{6\theta^3}\right)[1] & \frac{1}{\theta}[1] & [1] \end{bmatrix}, \tag{A33-3}$$

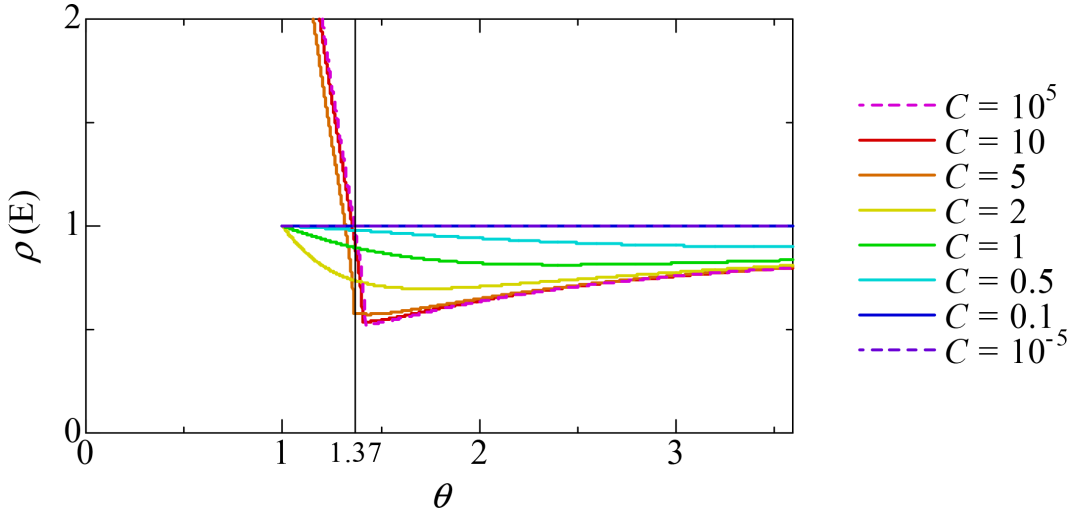
$$\mathrm{D} = \begin{bmatrix} \frac{1}{\theta}[1] & [0] & [0] \\ \frac{1}{2\theta^2}[1] & [0] & [0] \\ \frac{1}{6\theta^3}[1] & [0] & [0] \end{bmatrix}, \tag{A33-4}$$

10970207, 2025, 21, Downloaded from https://onlinelibrary.wiley.com/doi/10.1002/nme.70164 by Nagoya University, Wiley Online Library on [07/10/2026]. See the Terms and Conditions (https://onlinelibrary.wiley.com/terms-and-conditions) on Wiley Online Library for rules of use; OA articles are governed by the applicable Creative Commons License

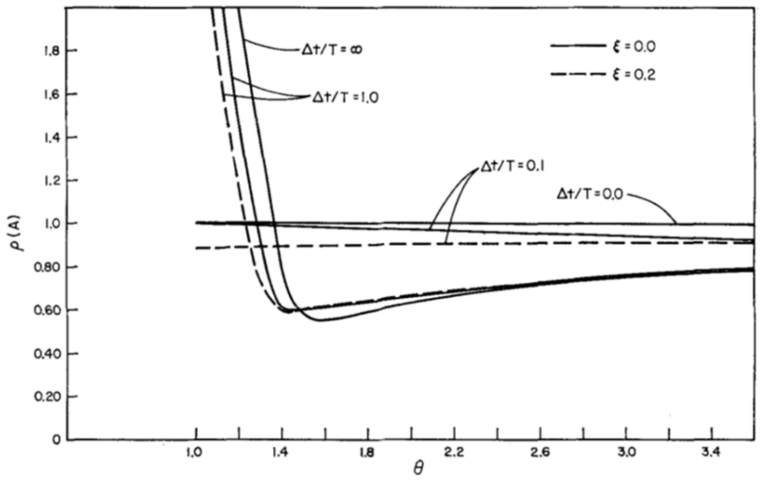
Analysis Results

The variation in the spectral radius of matrix E in Equation (A31) was analyzed by adjusting the value of in Wilson's method for various dimensionless wave celerities (C). For the other parameters, a single element (= 1) was used to represent a single-degree system, with a thickness of $\Delta = 1$, dimensionless time increment $\Delta = 1$, and dimensionless damping ratio $\Xi = 0$ (undamped condition). The analysis results obtained using the proposed method, shown in Figure A2a, demonstrated unconditional convergence ($(\rho(E) \le 1) \le 1$ for $\theta > 1.37$, regardless of C.

Additionally, a greater value of C means the smaller dimensionless period $T_n = \Lambda_n / C$ for the n-th eigenmode, with its dimensionless wavelength $\Lambda_n = 4/(2n-1)$—equivalent to a smaller dimensionless time increment relative to the representative time $\Delta T / T_n$. The analysis results obtained using the proposed method, shown in Figure A2a, displayed the same trend as the results (= 0.0, undamped case) presented by Bathe and Wilson [14] in Figure A2b, thus validating the proposed stability analysis method.



(a) Results obtained by proposed method



(b) Results appeared in Bathe and Wilson (1972)

FIGURE A2 | Spectral radius as a function of θ in Wilson method.

10970207, 2025, 21, Downloaded from https://onlinelibrary.wiley.com/doi/10.1002/nme.70164 by Nagoya University, Wiley Online Library on [07/10/2026]. See the Terms and Conditions (https://onlinelibrary.wiley.com/terms-and-conditions) on Wiley Online Library for rules of use; OA articles are governed by the applicable Creative Commons License